

Interactions between Convection and a Moist Vortex Associated with an Extreme Rainfall Event over Southern West Africa

MARLON MARANAN, ANDREAS H. FINK, AND PETER KNIPPERTZ

Karlsruhe Institute of Technology, Karlsruhe, Germany

SABASTINE D. FRANCIS

Nigerian Meteorological Agency, Abuja, Nigeria

ARISTIDE B. AKPO

Université d'Abomey-Calavi, Cotonou, Bénin

GBENGA JEGEDE

Obafemi Awolowo University, Ile-Ife, Nigeria

CHARLES YORKE

Ghana Meteorological Agency, Accra, Ghana


(Manuscript received 11 November 2018, in final form 29 March 2019)

ABSTRACT

An intense mesoscale convective system (MCS) in the Guinea Coast region caused one of the highest ever recorded daily rainfall amounts at the Nigerian station Abakaliki on 12 June 2016 (223.5 mm). This paper provides a detailed analysis of the meso- and synoptic-scale factors leading to this event, including some so far undocumented dynamical aspects for southern West Africa. The MCS formed over the Darfur Mountains due to diurnal heating, then moved southwestward along a mid- to lower-tropospheric trough, and developed into a classical West African squall line in a highly sheared environment with pronounced midlevel dryness. Strong moisture flux convergence over Nigeria prior to the MCS passage led to extreme values in precipitable water and was caused by the formation of a local, short-lived heat low. According to the pressure tendency equation, the latter resulted from tropospheric warming due to MCS-forced subsidence as well as surface insolation in the resulting almost cloud-free atmosphere. In this extremely moist environment, the MCS strongly intensified and initiated the formation of a lower-tropospheric vortex, which resulted in a deceleration of the MCS and high rainfall accumulation at Abakaliki. Following the vorticity equation, the vortex formation was realized through strong low-level vortex stretching and upper-level vertical vorticity advection related to the MCS, which became “dynamically large” compared to the Rossby radius of deformation. Eventually, moisture supply and lifting associated with the vortex are suggested to promote the longevity of the MCS during the subsequent westward movement along the Guinea Coast.

1. Introduction

Extreme rainfall has frequently struck West Africa in the past decade, causing considerable distress in the humanitarian, economic, and infrastructural sectors

 Denotes content that is immediately available upon publication as open access.

Corresponding author: Marlon Maranan, marlon.maranan@kit.edu

(Di Baldassarre et al. 2010; Nka et al. 2015). Particularly the wet monsoon season of 2007 and 2010 illustrated the enormous impacts of inundations due to extensive rainfall, with the former affecting over 1.5 million people in sub-Saharan Africa (WHO/WFP 2007; Paeth et al. 2011). Not least because of these events, a number of studies suggested a partial recovery of rainfall associated with the West African monsoon (WAM) following the droughts in the 1970s to 1990s (e.g., Nicholson 2005; Lebel and Ali 2009; Sanogo et al. 2015), although

DOI: 10.1175/MWR-D-18-0396.1

© 2019 American Meteorological Society. For information regarding reuse of this content and general copyright information, consult the [AMS Copyright Policy \(www.ametsoc.org/PUBSReuseLicenses\)](https://www.ametsoc.org/PUBSReuseLicenses).

with high spatiotemporal variability. The reasons for this are potentially linked to a change in the nature of daily precipitation. In a recent study for the central Sahel, [Panthou et al. \(2014\)](#) found an increasing trend of extreme rainfall days, while the overall number of rainy days has decreased. This is in accordance with studies on the global trend, which generally emphasize an increase in the frequency and intensity of extreme precipitation (e.g., [Easterling et al. 2000](#); [Alexander et al. 2006](#); [Trenberth et al. 2007](#); [Donat et al. 2013](#)).

Over West Africa, the majority of the WAM rainfall is known to be related to mesoscale convective systems (MCSs). From a climatological perspective, several studies suggest that MCSs account for up to 90% of annual rainfall in the Sahelian zone (e.g., [D'Amato and Lebel 1998](#); [Mathon and Laurent 2001](#); [Mathon et al. 2002](#); [Nesbitt et al. 2006](#)) and around 76% in the Soudano–Sahelian region to the south ([Fink et al. 2006](#)). Historical investigations on different rainfall types in the moister Guinea Coast region are rare and are mostly based on in situ rainfall recordings ([Acheampong 1982](#); [Omotsho 1984, 1985](#); [Kamara 1986](#)). Recent publications by [Janiga and Thorncroft \(2014\)](#) and [Maranan et al. \(2018\)](#), who used a multiyear high-resolution rainfall dataset from the precipitation radar onboard the Tropical Rainfall Measuring Mission (TRMM) satellite, have highlighted a decrease of the rainfall fraction attributable to MCSs from the Sahel toward the Guinea Coast (56% in [Maranan et al. 2018](#)).

Despite the aforementioned impacts of extreme rainfall events in West Africa, there is a dearth of studies investigating their dynamic controls. [Paeth et al. \(2011\)](#) addressed the 2007 sub-Saharan flood event and proposed a strong correlation between the excessive rainfall and anomalously strong low-level westerlies and a strong tropical easterly jet (TEJ), resembling typical conditions for positive rainfall anomalies in both the Guinea Coast and Sahel regions according to [Nicholson \(2009\)](#). Both factors are assumed to be conducive for the development of MCSs through enhanced upper-level divergence and low-level moisture transport, particularly when coupled with African easterly waves (AEWs) along the African easterly jet (AEJ). An exceptional event of extreme rainfall in West Africa was highlighted in the works of [Engel et al. \(2017\)](#) and [Lafore et al. \(2017\)](#), who investigated the Ouagadougou case of 2009. This event was affected by the “breaking” of the arguably strongest AEW in the 1974–2014 period and a subsequent formation of an intense mid- to low-tropospheric vortex, which led to excessive precipitable water (PW), a slow movement of the associated MCS and eventually the highest ever recorded rainfall amount at Ouagadougou with 263 mm. In general, such

midlevel vortices over West Africa have been described to be favorable for prolonged rainfall ([Fink et al. 2006](#)) due to prevailing widespread low-level convergence (e.g., [Acheampong 1982](#); [Buckle 1996](#)). However, the way such vortices interact with strong convection in association with extreme precipitation is not well understood. Few studies hinted toward a MCS–vortex interaction over West Africa. [Fortune \(1980\)](#) gave evidence of a midlevel vortex as part of an AEW that enhanced the squall line activity. In a modeling study, [Schwendike and Jones \(2010\)](#) showed that convection, associated with the precursor of Hurricane Helene 2006, was intensified through vortex stretching once midlevel vorticity anomalies had moved over a low-level cyclonic circulation.

The present paper addresses an extreme rainfall case on 12 June 2016 during the extensive field campaign Dynamics–Aerosol–Chemistry–Cloud Interactions in West Africa (DACCIWA) in June and July 2016 ([Knippertz et al. 2015, 2017](#)), which exhibited one of the highest ever recorded rainfall amounts in the Guinea Coast region. Comparable to the Ouagadougou case, it involved a long-lived MCS as well and a moist lower-tropospheric vortex. Based on several in situ measurements from the DACCIWA campaign as well as space-borne observations and the new reanalysis ERA5 of the European Centre for Medium-Range Weather Forecasts (ECMWF), this study examines the evolution and (thermo-) dynamical mechanisms of the MCS–vortex interaction in order to better understand the extreme nature of this rainfall event. An interesting aspect of this case is the fact that the MCS traversed the dry Savannah as well as the moister Guinea Coast region, which enables an analysis of environmental conditions associated with the longevity of the MCS for two contrasting regimes.

The manuscript is structured as follows: After a description of the data and methods in [section 2](#), an overview of the case with respect to cloud and rainfall measurements and its climatological context is given in [section 3](#). The next three sections address the environmental conditions and development of the MCS during the passage over the Savannah region in Chad ([section 4](#)), the passage over Nigeria ([section 5](#)), and finally a brief section about the westward movement along the Guinea Coast ([section 6](#)). A summary and conclusions are then provided in [section 7](#).

2. Data sources and methods

a. Global reanalysis data

A major part of this study is based on the fifth generation of the ECMWF Reanalysis (ERA5) ([Hersbach and Dee 2016](#)), successor of ERA-Interim (ERA-I;

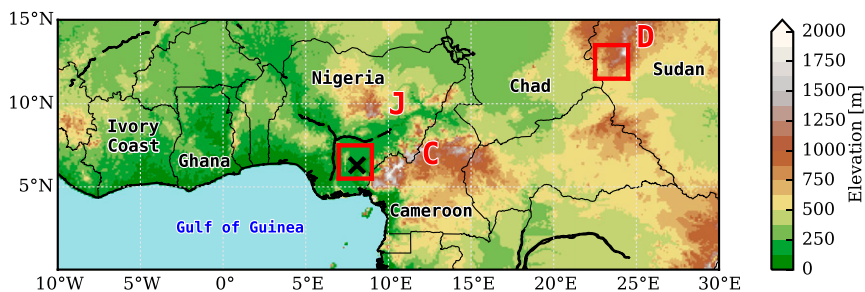


FIG. 1. Map showing central and West Africa. Shading denotes the terrain elevation as provided by the Global Land One-km Base Elevation Project (GLOBE) (Hastings et al. 1999). Countries mentioned in the text are indicated. Red capital letters denote the Darfur Mountains (D), Jos Plateau (J), and the Cameroon Highlands (C). The red boxes denote the area where spatial averages are performed in sections 4 and 5. The black \times mark indicates the location of the rain gauge station Abakaliki.

Dee et al. 2011). ERA5 is provided on an hourly basis and was taken at a 0.3° grid-spacing, close to its native resolution (0.28125°). By the time this manuscript was compiled, ERA5 was available only from 2000 to 2018. Thus, long-term means were computed for this 19-yr period. The fields are confined to the domain of study illustrated in Fig. 1. The virtual-temperature-corrected mixed-layer CAPE, CIN, and 650-hPa-based downdraft CAPE (DCAPE) were estimated from the reanalysis using vertical profiles based on 137 model levels in the ERA5 dataset. Here, DCAPE is used as a proxy for the strength of a convective cold pool (Emanuel 1994) and its potential capability of lifting air masses at the outflow boundary. Finally, diabatic heating rates from short-term forecasts produced as part of ERA5 are used to compute the diabatic heating term in the pressure tendency equation.

b. Cloud datasets

The cloud features of the MCS were tracked by applying an overlap-based tracking routine following Schröder et al. (2009) on 15-min infrared (IR) satellite data from the Spinning Enhanced Visible and Infrared Imager (SEVIRI) at a center-wavelength of $10.8\ \mu\text{m}$. SEVIRI is managed by the European Organisation for the Exploitation of Meteorological Satellites (EUMETSAT) and provides full-disk snapshots at a spatial resolution of approximately 3 km at nadir. A more detailed description of the procedure can be found in Schröder et al. (2009) and Maranan et al. (2018). The translation velocity of a convective system was obtained by calculating the spatial shift of the “center of mass” for the 233-K cloud top envelope divided by the temporal resolution of 15 min. Furthermore, a 2-h running mean was applied for smoothing purposes.

An analysis of the upper-tropospheric wind field was performed using atmospheric motion vectors from

EUMETSAT. We used the water vapor channel 5 with a center-wavelength of $6.2\ \mu\text{m}$, since the corresponding upper-level divergence product of EUMETSAT has currently been computed for this channel only (EUMETSAT 2015).

This study also makes use of spaceborne passive microwave (MW) radiometer datasets from the Microwave Humidity Sounder (MHS) and from the Sounder for Probing Vertical Profiles of Humidity (SAPHIR) on board Megha-Tropiques. Following Redl et al. (2015), only the 157-GHz channel of MHS is used for the analysis. SAPHIR operates near the 183.31-GHz water vapor absorption line. Specifically, the 183.31 ± 0.2 GHz channel corresponds to the observation of the 250–100-hPa layer (Subrahmanyam and Kumar 2013) and was therefore chosen for the analysis.

c. Rainfall and radiosonde datasets

The gridded Level-3 rainfall product of the Global Precipitation Measurement (GPM), termed the Integrated Multi-Satellite Retrievals for GPM (IMERG, Version 5), updates rainfall estimates every 30 min at a spatial resolution of 0.1° (Hou et al. 2014). IMERG is a blended product that consists of MW estimates as well as MW-calibrated IR estimates, if MW information is absent. Regional rainfall biases are then corrected by the incorporation of monthly rain gauge data (Huffman et al. 2015). Alongside IMERG, the present study uses daily rainfall information from over 150 rain gauge stations, which were collected during the DACCIWA campaign from several national weather services in the region.

Finally, vertical wind profiles from radiosonde launches during the DACCIWA campaign at the airports of Cotonou (Benin, WMO number: 65344), Abuja (Nigeria, 65125), and Enugu (Nigeria, 65257) were used to investigate prestorm conditions (Maranan and Fink 2016).

We note that radiosonde data of Abuja and Enugu are not disseminated operationally through the Global Telecommunication System (GTS) and are therefore not assimilated in reanalysis data such as ERA5.

d. Pressure tendency and vorticity equation

In this study, we follow the pressure tendency equation (PTE) description of Fink et al. (2012), but based on hourly changes (i.e., between t_{-1h} and t_0):

$$\begin{aligned} \frac{\partial p_{\text{sfc}}}{\partial t} &= \rho_{\text{sfc}} \left(\frac{\partial \phi_{p_2}}{\partial t} \right) & (D\phi) \\ &+ \rho_{\text{sfc}} R_d \int_{\text{sfc}}^{p_2} \left(\frac{\partial T_v}{\partial t} \right) d \ln p & (\text{ITT}) \\ &+ g(E - P) & (\text{EP}) \\ &+ \text{RES}_{\text{PTE}}, & (1) \end{aligned}$$

where p_{sfc} is the surface pressure, ρ_{sfc} the air density at surface level, R_d the gas constant of dry air, T_v the virtual temperature, and g the acceleration of gravity. The upper boundary p_2 was chosen to be 100 hPa. The four terms on the right-hand side affecting the pressure tendency (Dp) are the temporal change in upper boundary geopotential ($D\phi$), the vertically integrated temperature tendency (ITT), the net mass change due to precipitation P and evaporation E (EP), and a residual term due to spatiotemporal interpolation and discretization (RES_{PTE}).

The ITT term, in turn, can be expanded as

$$\begin{aligned} \text{ITT} &= \rho_{\text{sfc}} R_d \int_{\text{sfc}}^{p_2} -\mathbf{v}_h \cdot \nabla_p T_v d \ln p & (\text{TADV}) \\ &+ \rho_{\text{sfc}} R_d \int_{\text{sfc}}^{p_2} \left(\frac{R_d T_v}{c_p p} - \frac{\partial T_v}{\partial p} \right) \omega d \ln p & (\text{VMT}) \\ &+ \rho_{\text{sfc}} R_d \int_{\text{sfc}}^{p_2} \left(\frac{T_v \dot{Q}}{c_p T} \right) d \ln p & (\text{DIAB}) \\ &+ \text{RES}_{\text{ITT}}, & (2) \end{aligned}$$

where \mathbf{v}_h and ω are the horizontal and vertical wind components, respectively, c_p is the specific heat capacity for isobaric processes, T the air temperature, p the air pressure, and \dot{Q} the diabatic heating rate. The surface pressure can be modified due to horizontal temperature advection (TADV), vertical motion (VMT), diabatic processes (DIAB), and spatiotemporal discretization errors (RES_{ITT}). Here, DIAB is calculated from the diabatic heating rates provided in the ERA5 short-term

forecasts. We refer to Knippertz and Fink (2008) and the supplemental material of Fink et al. (2012) for the derivations of the PTE and ITT as well as a detailed explanation of the terms.

The vorticity equation (VTE) in isobaric coordinates can be expressed as (see, e.g., Holton and Hakim 2012)

$$\frac{\partial \zeta}{\partial t} = \underbrace{-\mathbf{v}_h \cdot \nabla \eta}_{\text{HADV}} - \underbrace{\omega \frac{\partial \zeta}{\partial p}}_{\text{VADV}} - \underbrace{\eta \nabla \cdot \mathbf{v}_h}_{\text{DIV}} + \underbrace{\mathbf{k} \cdot \left(\frac{\partial \mathbf{v}_h}{\partial p} \times \nabla \omega \right)}_{\text{TILT}}, \quad (3)$$

where ζ , f , and $\eta = \zeta + f$ are the relative, planetary, and absolute vorticities, respectively, \mathbf{k} is the vertical unit vector, and the other variables are as in Eqs. (1) and (2). The first and second term on the right-hand side of Eq. (3) are the horizontal (HADV) and vertical advection (VADV) of absolute vorticity, respectively. The third term, also known as stretching term, describes the change of vorticity through divergence (DIV). Finally, the fourth term represents changes in ζ due to an inhomogeneous vertical motion field and is also called tilting term (TILT).

3. Cloud and precipitation features of the extreme event

On 12 June 2016, the weather station in Abakaliki in the southeastern part of Nigeria reported 223.5 mm in 24 h, one of the highest daily rainfall sums ever recorded at near-coastal stations in West Africa (not shown). The analysis of the IR-based tracking reveals that this rainfall event was caused by a long-lived MCS (Fig. 2a). It formed in the afternoon of 10 June over the Darfur Mountains in western Sudan from where it grew rapidly, and swiftly moved toward the southwest at an approximate peak translation velocity of 18.3 ms^{-1} along the track. Arriving over Nigeria in the evening of 11 June, the MCS quickly intensified, characterized not only by colder minimum cloud top temperatures below 190 K in the IR band, but also by an overall increased area, particularly extending farther to the north (Fig. 2a). The latter is indicated by the northward shift of the MCS track. We note that such abrupt changes in the direction of the track may appear somewhat unrealistic and are, in this case, a consequence of a merging convective cell at the northern edge of the MCS. During 12 June, the MCS reached the northern Gulf of Guinea and moved farther west along the Guinea Coast. The minimum temperature anywhere in the cloud top rose as soon as the MCS moved over open water (see color scheme of the track), indicating a cloud system of lower vertical extent. Furthermore, the translation velocity of the MCS decreased to 11.2 ms^{-1} . By early 13 June, another turn in the track

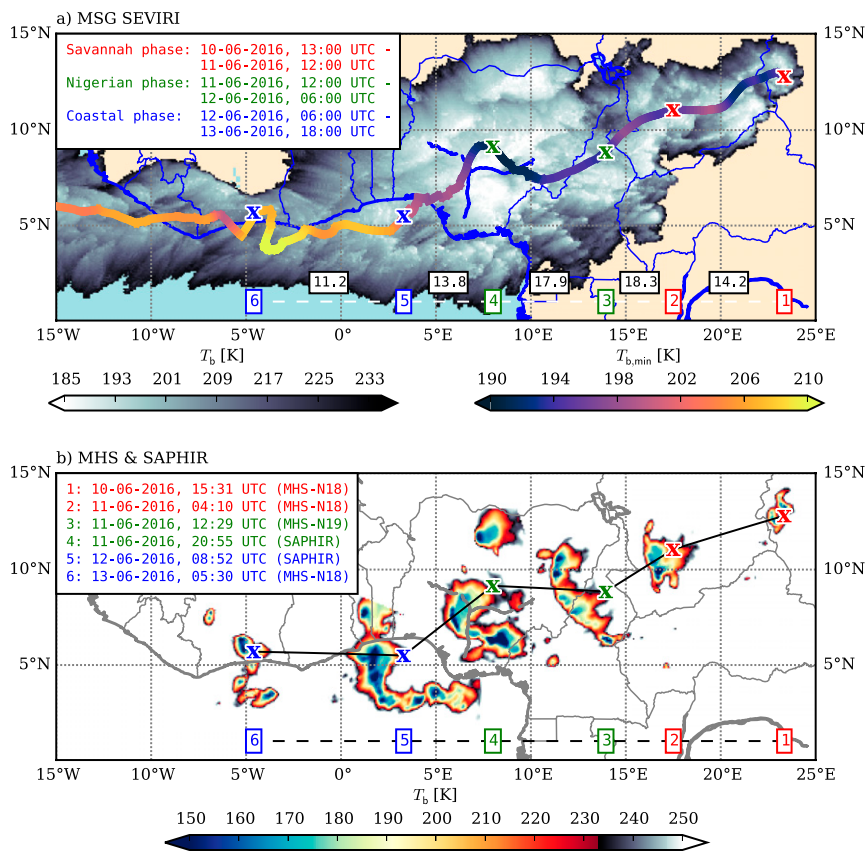


FIG. 2. Composites of the cloud characteristics of the MCS. (a) The grayscale shading denotes the spatial extent of the MCS as well as the IR brightness temperature. The track of the weighted center of mass of the MCS is shown as a thick line, where the colors indicate the minimum SEVIRI IR brightness temperature of the MCS $T_{b,min}$ anywhere in the cloud top at the respective time steps. The colored markers along the track refer to the colored numbers at the bottom, which in turn correspond to snapshots of the MCS as seen in (b). The marker colors refer to the legend, where the different phases of the MCS are named (see the respective sections for more details). The values between the snapshot numbers indicate the translation velocity (in m s^{-1}) of the MCS between the respective snapshots. (b) Snapshots from MW channels of MHS and SAPHIR of key stages in the MCSs' lifetime, which are numbered at the bottom as in (a). Note that different MW frequencies are used between MHS and SAPHIR (see section 2). The textbox in the upper left corner indicates the day and time of overpass, colored according to the MCS phases.

is visible over Ivory Coast (Fig. 2a). It is associated with the development of new convective cells in the wake of the decaying MCS (not analyzed in this study), which caused high rainfall amounts particularly at the coastal stations in Axim (Ghana, 114.8 mm) and Abidjan (Ivory Coast, 106.2 mm). These new convective cells led to a continuation of the track of the cloud cluster toward the eastern Atlantic (not shown).

In Fig. 2b, six MW-based snapshots of the MCS development are shown. During its southwestward propagation, the MCS evolves from small convective clusters (snapshot 1, see textbox in Fig. 2b for dates and times) to a moderately (snapshot 2) and eventually highly organized and well-defined squall line (snapshot 3). As it

intensifies over Nigeria, the MCS deforms and features two connected convective cores (snapshot 4). It is the intense southeastern core that caused the extreme rainfall over Abakaliki. Successive IR cloud images around 2000 UTC 11 June (not presented here), show the merging of smaller convective cells embedded the MCS over the Abakaliki region, which ultimately form this intense core at snapshot 4. At snapshot 5, the MCS has moved over the ocean and features a pronounced tail at the southern flank (Fig. 2b). The latter, however, is not the remainder of the Abakaliki core, but rather a consequence of dynamical characteristics described in section 6. Eventually, snapshot 6 illustrates both the fragments of the decaying MCS to the

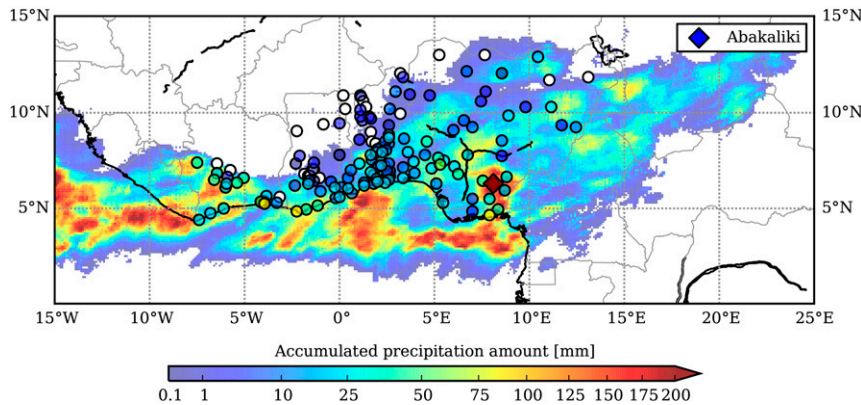


FIG. 3. Precipitation composite of the IMERG estimated total rainfall (color shaded) produced within the 233-K envelope of the MCS (see Fig. 2a). The color-filled circles show the daily rainfall amount at various stations over West Africa at the day of the MCS overpass. We note that the overpass falls within two reporting periods at some stations, that is, including the change of the measurement day at 0600 UTC (except for Ghana at 0900 UTC). The higher value out of the two days is taken in this case.

south as well as a new convective cell at the northern edge, which leads to the abovementioned unrealistic loop in the track.

The period between 11 and 13 June 2016 marked the wettest spell of the entire DACCWA period at the Guinea Coast. This wet spell was associated with a mobile vortex subjectively identified from 850-hPa streamlines and labeled “feature B” in Knippertz et al. (2017). Figure 3a shows the accumulated IMERG rainfall (shaded) within the MCS’s envelope (see Fig. 2a) and the rainfall sum measured by affected rain gauge stations on the day of the overpass. Along the MCS path, several distinct rainfall swaths are visible, particularly east of 10°E during the squall line stage. High IMERG rainfall around 200 mm is seen over the Abakaliki region in southeastern Nigeria, consistent with the associated station value of 223.5 mm (diamond marker). Considering the substantially lower precipitation amounts at stations close to Abakaliki, it becomes apparent how localized the extreme event was. More than 100 mm were recorded only at the aforementioned stations at Axim and Abidjan west of the 0° meridian.

In the following, we analyze three phases in the MCS development (see also the textbox in Fig. 2a). The first phase, “Savannah phase,” refers to the period from formation until the arrival of the MCS in Nigeria as a squall line (1300 UTC 10 June–1200 UTC 11 June) (section 4). The following “Nigerian phase” addresses the intensification phase of the MCS over Nigeria (1200 UTC 11 June–0600 UTC 12 June) (section 5). The last phase, termed the “coastal phase” (0600 UTC 12 June–1800 UTC 13 June),

discusses the evolution of the MCS during its westward migration along the Guinea Coast (section 6).

4. The Savannah phase (SP)

a. Regional-scale setting and initiation

The regional-scale dynamical setting around the MCS period is described in detail in the DACCWA overview paper by Knippertz et al. (2017). It was characterized by the presence of the Saharan heat low in its intense phase, which was located anomalously far north with associated low-level southwesterlies penetrating deep into the eastern Sahel. This development may have provided western Sudan with sufficient moisture prior to the MCS formation. Being anomalously weak and far south in the beginning of June, the AEJ started to intensify and to gradually migrate northward. It was located over southern Chad on 7 June 2016, creating a zone of strong low-level wind shear over the region.

Within this environment, the MCS formed around 1400 UTC 10 June over the Darfur Mountains, which is generally a prominent region for convective initiation (Berry and Thorncroft 2005; Mekonnen et al. 2006; Laing et al. 2008). Based on Fig. 4, where the box-averaged (thermo-)dynamical conditions over the Darfur Mountains (easternmost red box in Fig. 1) are shown between 36 h before and after the time of initiation (black vertical line), MCS formation is suggested to be a consequence of diurnal heating at elevated terrain. Necessary conditions such as the buildup of CAPE and the breakdown of CIN during daytime (Fig. 4a) reflect high conditional instability, which is consistent with observed diurnal rainfall in

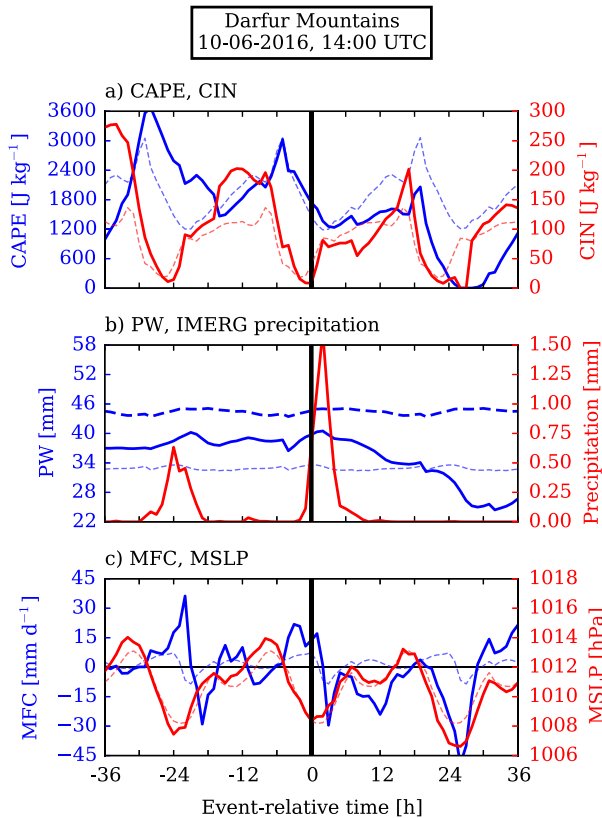


FIG. 4. Environmental conditions averaged over the $2^\circ \times 2^\circ$ box over the Darfur Mountains (see Fig. 1) in a ± 36 h window centered around the formation of the MCS (black vertical line) at 1400 UTC 10 Jun 2016. The metrics are (a) CAPE and CIN, (b) precipitable water (PW) and hourly IMERG rainfall, and (c) column-integrated moisture flux convergence (MFC) and mean sea level pressure (MSLP). Thin dashed lines in all panels show the long-term (2000–18) mean June values at the respective hour. The thick dashed line in (b) indicates the hourly 99th percentile of PW for June based on the same 19-yr ERA5 dataset as for the long-term mean.

IMERG (Fig. 4b). During the formation, both CAPE and CIN exhibit similar values compared to the long-term mean (thin dashed lines). PW, in turn, is higher than normal and likely to be a consequence of the aforementioned far reaching monsoon flow. However, PW is not extreme when compared to the 19-yr-based 99th percentile (thick dashed line in Fig. 4b). Small variations in PW before MCS initiation largely result from fluctuations in the column-integrated convergence of moisture flux (MFC, Fig. 4c). MFC emerges from changes in mean sea level pressure (MSLP), which are most likely thermally driven. Overall, MCS initiation falls in the period of lowest MSLP and CIN as well as moderate MFC. This is supported by the fact that in ERA5 data, a diurnal rainfall pattern similar to IMERG is also visible (not shown).

b. The squall-line stage

A key factor for the development of the MCS into a highly organized system is its subsequent migration toward the southwest. The conditions along the MCS's path from snapshot 1 to 3 (see Fig. 2b) are illustrated in Fig. 5a. To analyze prestorm conditions, the variables were calculated for a moving $2^\circ \times 2^\circ$ box along the track, timed 2 h prior to the arrival of the MCS.

CAPE and PW gradually increase along the path compared to the initial point at snapshot 1 at 1300 UTC. The first increase of PW is a direct consequence of the southward migration into a moister regime, as indicated by the rise of the long-term mean (thin dashed line), resulting in higher CAPE values. The low-level wind shear (LLWS hereafter), which is approximated with the magnitude of the vector difference between the 600- and 925-hPa layer (cf. Laing et al. 2008), starts to strengthen toward the evening and night. Its relevance for the organization and longevity of MCSs has been already highlighted in earlier modeling and observational studies (e.g., Weisman and Klemp 1982; Barnes and Sieckman 1984). It is linked with enhanced storm-relative momentum and moisture transport into the cloud system as well as lifting along a convective cold pool (e.g., Rotunno et al. 1988; LeMone et al. 1998). The strength of the latter is estimated here by the 650-hPa-based DCAPE, which exhibits values around 900 J kg^{-1} (Fig. 5a), owing to dry midlevels over southern Chad (not shown). This is equal to a theoretical maximum downdraft velocity of $w = \sqrt{2\text{DCAPE}} \approx 42 \text{ m s}^{-1}$. However, whether this process helped to enhance the MCS's longevity is not entirely clear since ERA5 does not resolve it, but might have been a mechanism to overcome increasing CIN toward the night (Fig. 5a).

Between the snapshot locations 2 (0200 UTC) and 3 (1000 UTC), where the MCS develops into a squall line, CAPE and LLWS increase further above their long-term means (Fig. 5a). The latter is modulated by a trough in the low- and midtropospheric mean flow. Figure 5b shows the 600–950-hPa mass-weighted flow (blue streamlines, $V_{600-950}$ hereafter, cf. Lafore et al. 2017) as well as the magnitude of LLWS (shaded) and the 925-hPa flow (vectors) at the time when the MCS is located at snapshot 2 (0400 UTC 11 June 2016). Following $V_{600-950}$, the MCS is embedded in a region of pronounced northeasterlies within the trough. Considering the time of day, the higher magnitude of LLWS between snapshot 2 and 3 is a product of both northeasterlies and the undercutting nocturnal low-level jet (NLLJ) from westerly directions (e.g., Parker et al. 2005; Lathon et al. 2008; Knippertz et al. 2011; Schrage and Fink 2012), as seen in the 925-hPa flow. The NLLJ accounts for most of the moisture transport into the

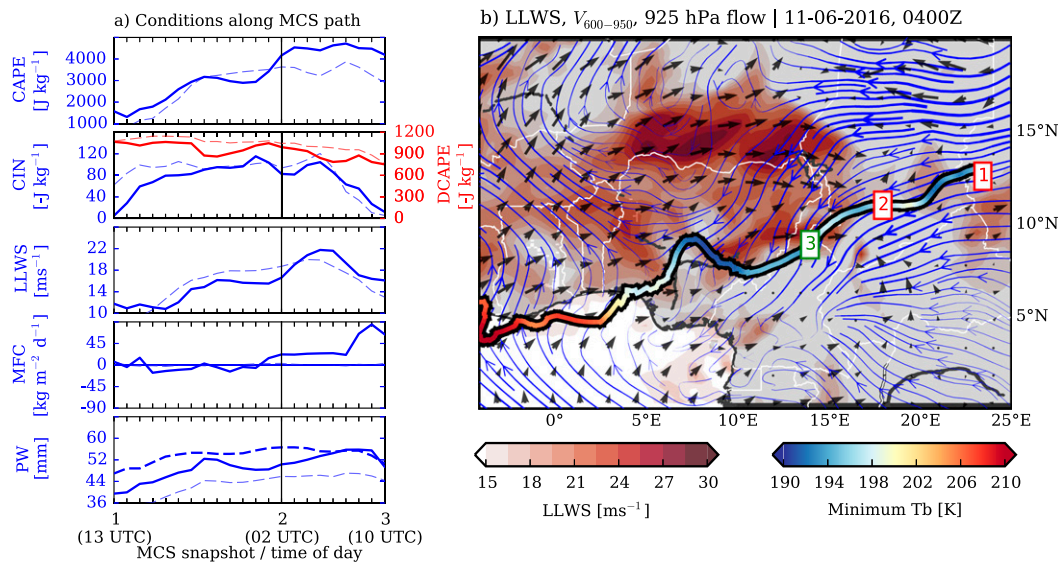


FIG. 5. (a) Environmental conditions along the MCS track between MCS snapshot locations 1 and 3 [see Fig. 2 or (b) for the positions of the snapshots on the track and the track itself]. The values indicate the instantaneous conditions 2 h prior to the arrival of the MCS and thus represent snapshots moving with the track. The respective time of day is indicated. The thin and thick dashed lines are as in Fig. 4. (b) Instantaneous fields for LLWS (shaded above 15 m s^{-1}), the 600–950-hPa mass-weighted flow ($V_{600-950}$, blue streamlines), and the 925-hPa flow (vectors) at 0400 UTC 11 Jun 2016, corresponding to the actual arrival time of the MCS at snapshot location 2. Here, the colored numbers on the track show the locations of the MCS at snapshots 1–3. The color code on the track line denotes the minimum IR-based cloud-top brightness temperature.

continent (Parker et al. 2005). There is some evidence that the NLLJ is also enhanced by being channeled in the Benue valley between the orographic features of the Jos Plateau and Cameroon Highlands (8° – 9° N, 10° – 15° E, see also Fig. 1 for geographical reference), which may have influenced the increase in MFC and, as a consequence, the increase in PW between snapshot 2 and 3 (Fig. 5a). Here, PW becomes extreme by reaching the 99th percentile. Together with the gradual breakdown of CIN, all these factors most likely facilitated the organization of the MCS into a squall line. Furthermore, the increase of LLWS between snapshot 2 and 3 coincides with an increase in translation speed of the MCS (Fig. 2a), indicating the typical motion characteristics of squall lines within LLWS-dominated front-to-rear storm-relative winds (Markowski and Richardson 2011).

5. The Nigerian phase (NP)

a. Intensification of the MCS

Similar to Fig. 4, an analysis of the dynamical and thermodynamical metrics around the arrival of the MCS (1800 UTC 11 June 2016) is performed in Fig. 6, but over the Abakaliki region (see Fig. 1). In the absence of clear diurnal oscillations, unlike during SP, a high-CAPE-low-CIN environment is generally found. Most notable

is a sharp increase of CAPE together with an almost complete removal of CIN around 6 h before the passage. The CAPE maximum is a result of both diurnal heating and a peak in near-surface humidity in the 72-h window (not shown). However, no rainfall is detected until 2 h before the passage of the MCS core (Fig. 6b). Just before the passage, PW experiences a pronounced increase and clearly surpasses its 19-yr-based 99th percentile in the process. Eventually, the box-averaged rainfall rate estimated by IMERG peaks at almost 18 mm h^{-1} during the overpass. The rise in PW is associated with an extreme MFC that peaks at over 140 mm day^{-1} (Fig. 6c), which is associated with prolonged rainfall in the ERA5 data (not shown). This MFC peak is related to a distinct surface pressure fall, which itself is linked to a semi-diurnal pressure fluctuation. Compared with long-term averaged variations of the MSLP (thin dashed red line), the present MSLP fall is not exceptionally stronger. However, further inspection of the horizontal MSLP field shown in Fig. 7a (1500 UTC 11 June) reveals a local MSLP minimum in the Abakaliki region, which results in a low-level inflow, as indicated by the 925-hPa flow. The existence of the MSLP depression is also evident from wind measurements (Fig. 7b). Vertical wind profiles from radiosonde launches at 1200 UTC 11 June at the surrounding stations Cotonou, Abuja and Enugu (see section 2) are plotted in a hodograph.

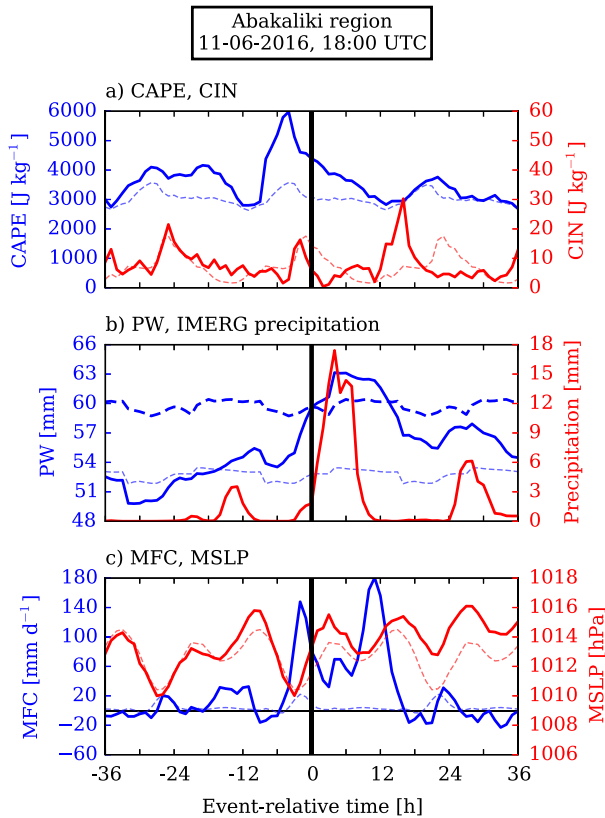


FIG. 6. As in Fig. 4, but for the Abakaliki box (see Fig. 1) centered around the start of the MCS passage at 1800 UTC 11 Jun.

The wind profile at Enugu (purple curve), the closest station to Abakaliki (see map inset), exhibits a cyclonic rotation at low levels before turning into strong northeasterlies above around 700 hPa. The latter might indicate the upper boundary of the low pressure system. At Cotonou (green curve), almost exactly to the west of Abakaliki, the wind profile is nearly zonal at all levels up to 600 hPa. Westerlies prevail at low levels and easterlies above 800 hPa. Low-level northwesterlies were present at Abuja (blue curve) to the north of Abakaliki before the flow again turned easterly at higher levels.

To investigate the causes behind the formation of the low, the PTE [see Eq. (1)] was applied to the same box over the Abakaliki region as in Fig. 6. Figure 8a shows hourly changes of the magnitude of the PTE components over the course of 11 June. Components calculated with the ERA5 reanalysis are denoted with “(A)” in the legend. The evolution of the pressure tendency at the surface Dp (solid black line) is characterized by a semidiurnal fluctuation with a net pressure fall starting at 0900 UTC that eventually leads to the MSLP minimum at 1500 UTC (green vertical shading). The pressure fall is mainly controlled by ITT,

which is sometimes compensated and sometimes supported by $D\phi$. Contributions from EP are negligible and tend to coincide with higher RES_{PTE} . Thus, the PTE is almost closed by $D\phi$ and ITT alone. Further inspection of the components of the ITT term [see Eq. (2)] is performed in Fig. 8b. ITT is evaluated using the ERA5 forecast dataset [denoted with “(F)”] since only this dataset contains the temperature tendencies due to parameterizations. Here, the forecast is able to reproduce the episode of pressure fall (dashed black curve in Fig. 8a). Within the ITT, the radiation part of DIAB can be calculated explicitly for shortwave ($DIAB_{SW}$) and longwave radiation $DIAB_{LW}$, respectively. Thus, the remainder of DIAB can be attributed to temperature changes due to latent and sensible surface heat fluxes and friction and is termed $DIAB_{dyn}$ hereafter. We find two characteristics that do not change much over time. First, $DIAB_{LW}$ is always positive around a value of 0.4 hPa h^{-1} and can be attributed to the cooling effect of terrestrial longwave radiation. Second, the influence of TADV is small, which is not surprising considering the rather small spatiotemporal variations in the temperature field in tropical environments. $DIAB_{dyn}$ usually counteracts VMT, particularly during the MCS passage from 1800 UTC onward. The positive VMT, associated with strong lifting inside the MCS and thus adiabatic cooling, is largely balanced by latent heat release within $DIAB_{dyn}$. However, during the period of pressure fall, both are mostly negative with $DIAB_{dyn}$ exhibiting rather small values. Moreover, the negative pressure tendency is further enhanced by $DIAB_{SW}$. Solar radiation ($DIAB_{SW}$) appears to warm the tropospheric column immediately after sunrise at 0600 UTC and is the strongest contributor to the pressure fall with a peak tendency of -0.8 hPa h^{-1} .

This development may be explained by upper-level dynamics. The upper-tropospheric divergence and wind fields derived from cloud motion vectors for 1345 UTC 11 June, approximately an hour before the MSLP minimum, are presented in Figs. 9a,b, respectively. In general, convective systems are a source of divergence (Fig. 9a, black contours), while cloud-free regions are usually associated with convergence (stippled blue contours). The latter is present over large parts of central and southern Nigeria. The location of the developing pressure minimum in ERA5 (green diamond marker) was embedded in this almost cloud-free region. Based on the spatial distribution of divergent motions, the region of convergence was created by surrounding convection to the north and south and by the approaching squall line to the east. Furthermore, the wind field in Fig. 9b indicates enhanced wind speeds

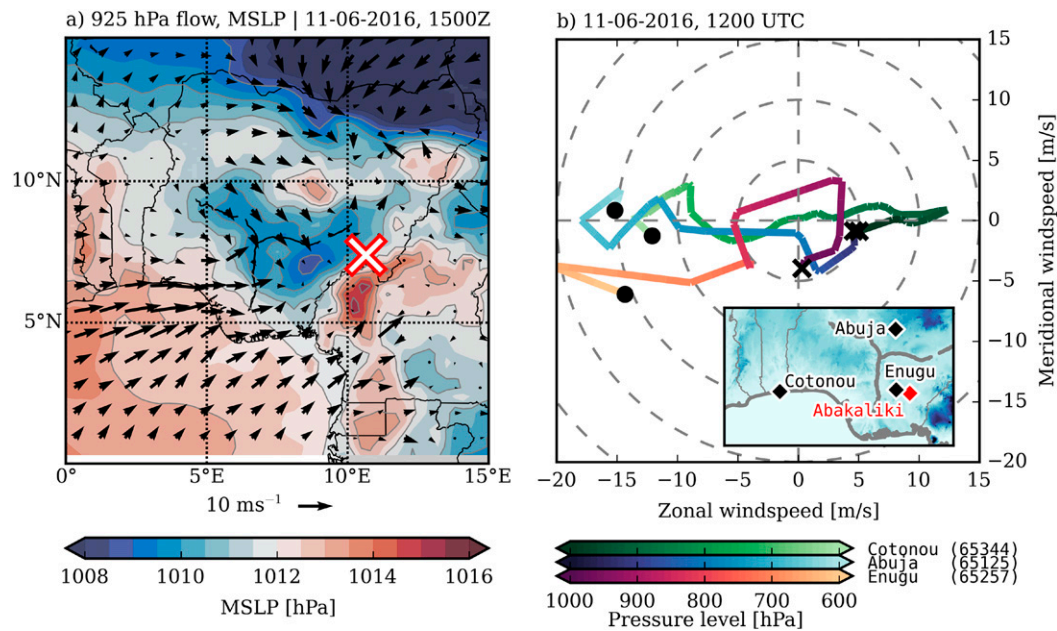


FIG. 7. (a) Mean sea level pressure field (shaded) and 925-hPa flow (vectors) at 1500 UTC 11 Jun 2016. The marker denotes the location of the MCS's center of mass. (b) Hodographs deduced from radiosonde wind data at Cotonou, Abuja, and Enugu at 1200 UTC 11 Jun 2016. Black cross markers indicate the lowest, black dots the highest altitude. The hodographs are cut at around 600 hPa. The map on the lower right shows the location of the radiosonde sites and Abakaliki.

of over 40 kt ($1 \text{ kt} \approx 0.5144 \text{ m s}^{-1}$) (blue shading) to the west of the MCS. This is most likely related to the strong outflow of the MCS, further enhancing the easterly flow related to the TEJ. It shall be stressed, however, that the area of convergence over central Nigeria is less pronounced than that over other regions with little cloud cover (e.g., at 10°N , 5°W in Fig. 9a). So the question remains if it would have been present at all were it not for the approaching intense squall line and its outflow. Combining these findings with Fig. 8b, we suggest that the MSLP minimum formed during a period of subsidence in an overall statically stable column (i.e., negative VMT) due to upper-level convergence, which in turn suppressed cloud formation and allowed insolation to further warm the tropospheric column (negative DIAB_{SW}). The net subsidence assumedly prevented strong convection to form prematurely despite the simultaneous buildup and removal of CAPE and CIN around this time step, as mentioned earlier (cf. Fig. 6a).

b. Moist vortex

The low pressure system over the Abakaliki region, which extends vertically to around 700 hPa (see Fig. 7b), promoted a strong increase in MFC (Fig. 6c) and supported the local intensification of the MCS in an extremely moist environment. This development most probably triggered a substantial deformation in

the low-level flow. Figure 10 shows the fields of PW, moisture flux, and the 700–950-hPa mass-weighted flow ($V_{700-950}$) during the passage of the MCS (0200 UTC 12 June). $V_{700-950}$ indicates a cyclonic vortex with its center being located over the Abakaliki region. This vortex manifests itself already several hours earlier [i.e., at around 2200 UTC 11 June (not shown)], and coincides with the development of the intense convective core at snapshot 4 in Fig. 2b. Convergent moisture flux vectors result in high MFC around the vortex center (Fig. 10), which in turn leads to an extensive region of high PW.

To evaluate possible mechanisms behind the vortex formation, the VTE was applied on the $2^\circ \times 2^\circ$ box over the Abakaliki region during the observed passage of the MCS (1800 UTC 11 June–0600 UTC 12 June). We stress that by using a global reanalysis dataset, the VTE will not capture the effects of small-scale vorticity sources and sinks (i.e., eddy fluxes) (cf. Sui and Yanai 1986; Davis and Galarneau 2009), and is one reason why the VTE could not be entirely closed (not shown). Given the size of the MCS and its clear representation in ERA5 (e.g., Fig. 8), emphasis is put onto the resolved mesoscale response. The upper row of Fig. 11 shows vertical profiles of relative vorticity ζ (solid black lines), divergence δ (dark gray dashed lines), and vertical velocity w (light gray dashed-dotted lines) at four different time

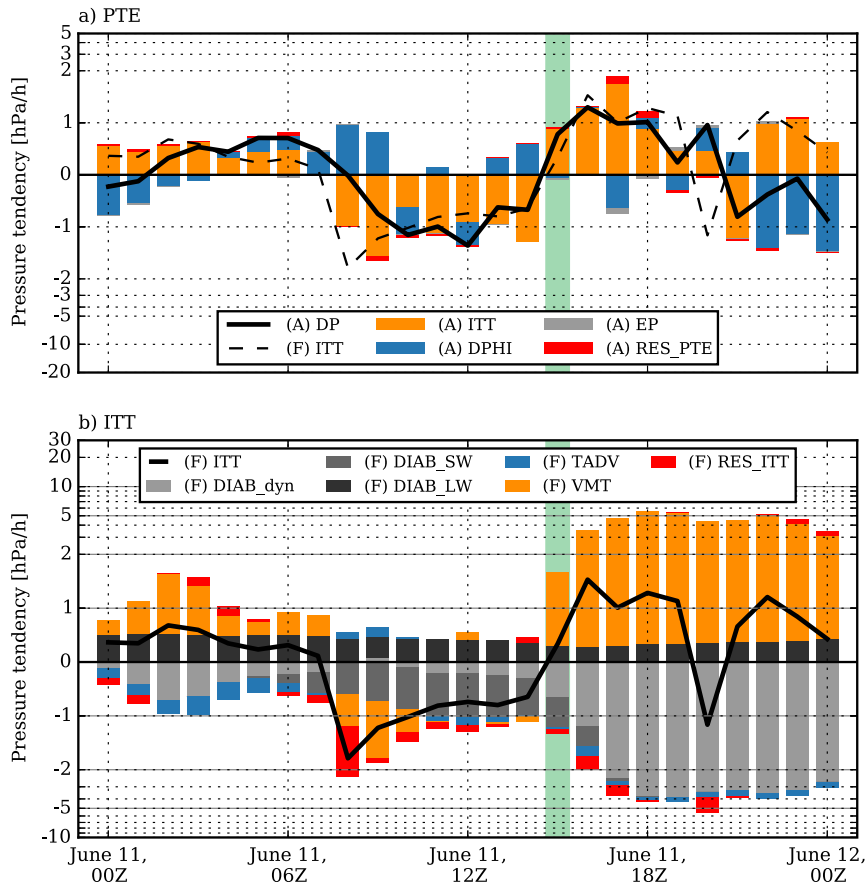


FIG. 8. (a) Hourly contribution of the PTE components (bars) to changes in MSLP from the ERA5 reanalysis (A) and ERA5 forecast (F). The black solid and dashed lines denote the net hourly change of MSLP and the ITT of the forecast, respectively. The green shading marks the time of the MSLP minimum, also indicated in (b). (b) Hourly contribution of the ITT components (bars) to changes in MSLP. The black solid line denotes the net hourly contribution of ITT. Only the forecast dataset (F) is used here.

steps. The ζ profiles indicate upward development of the cyclonic flow with a subsequent strengthening and deepening. On 0200 UTC 12 June, the vortex is fully visible in the mass-weighted flow (Fig. 10) and closed streamlines are found up to 700 hPa (not shown). At this time, cyclonic vorticity reaches up to 300 hPa (Fig. 11c) and is further enhanced by 0600 UTC 12 June (Fig. 11d). As a consequence of the heat low, the low-level flow is convergent prior to the MCS's arrival (Fig. 11a), but deepens throughout the MCS passage as the vortex forms. Divergence, in turn, is mainly found at upper levels resulting from the convective outflow, accompanied by an enhanced mesoscale vertical velocity up to around 0.4 m s^{-1} at 300 hPa (Fig. 11d). Figures 11e–h illustrate the contributions of the VTE components to the net change in relative vorticity $D\zeta$ (black line) at the respective time steps. In principle, the maxima of positive $D\zeta$ exhibit a gradual upward

migration, leading to the deep layer of positive ζ . It coincides with an upward development of the horizontal vorticity advection (HADV), which is primarily caused by the synoptic-scale trough. Thus, the delayed passage of the trough axis, leading to the HADV maxima at subsequently higher altitudes, reflects the baroclinic nature of the wave. While HADV initially contributes to the deepening of the positive ζ -layer (Fig. 11g), it is fully balanced by the divergence term (DIV) at all levels toward the end of the MCS passage (Fig. 11h). In general, anticorrelated VTE components (HADV-DIV, VADV-TILT) appear to be a typical feature, once the vortex is created, comparable to studies that investigate mesoscale convective vortices in midlatitudes (e.g., Kniewel and Johnson 2003). At low levels, HADV reacts to the column stretching produced by DIV. The latter starts to strengthen at 0200 UTC 12 June, in the 800–900-hPa layer (Fig. 11g) and deepens up to

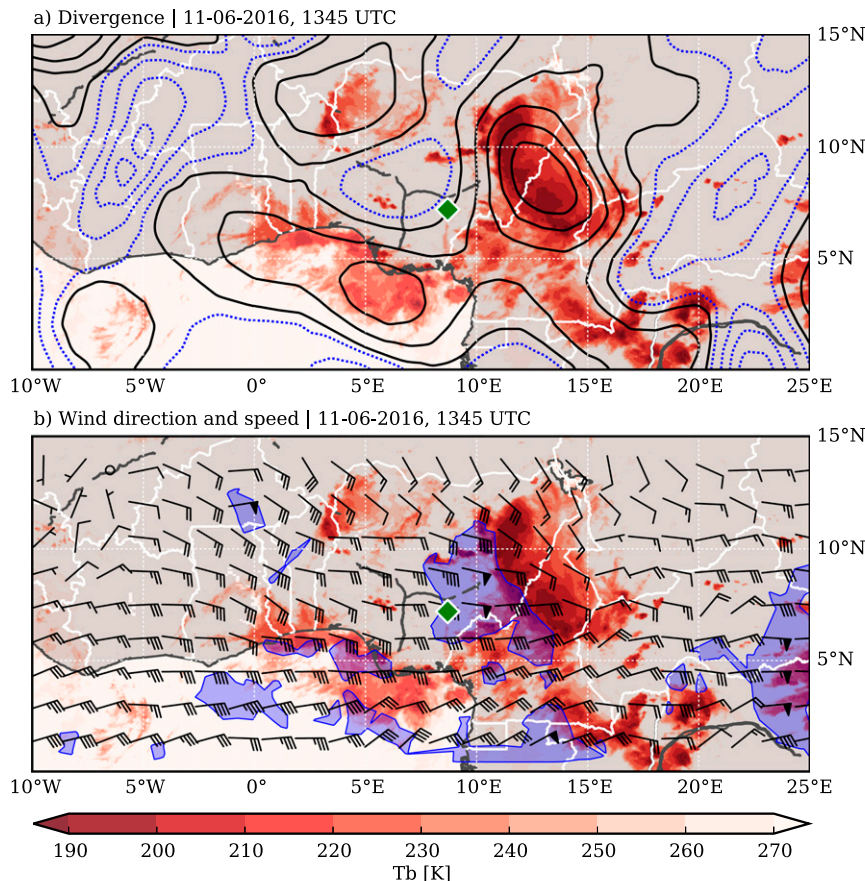


FIG. 9. Upper-level motion fields at 1345 UTC 11 Jun 2016, derived from the SEVIRI 6.2- μm water vapor channel (channel 5). (a) Divergence (black contours) and convergence (dotted blue contours) are plotted over cloud features below 270 K (red shadings). The contours start at $\pm 0.25 \times 10^{-5} \text{ s}^{-1}$ incremented by $\pm 10^{-5} \text{ s}^{-1}$. The green diamond marker denotes the location of the MSLP minimum of Fig. 7a. (b) Upper-level wind field (barbs) together with areas of $>40 \text{ kt}$ (light blue shadings).

500 hPa at 0600 UTC (Fig. 11h). With the vortex center in the box, any inflow results in a negative tendency of HADV. The vertical vorticity advection VADV generally cancels TILT at low levels, but outweighs it in the layer above 600 hPa (Fig. 11h). Thus, VADV strongly contributes to the positive $D\zeta$ in this layer. Overall, the development of the vortex appears to be a result of the strong latent heat release within the intensified MCS, leading to column stretching in the lower and pronounced vertical vorticity transport in the upper troposphere, respectively.

The importance of the MCS to the vortex formation is further emphasized when considering the geometrical size of the MCS compared to the Rossby radius of deformation λ_R , defined as

$$\lambda_R = \frac{NH}{(\zeta + f)^{1/2}(2VR^{-1} + f)^{1/2}}, \quad (4)$$

where N is the Brunt–Väisälä frequency, H the scale height of the circulation (i.e., the vortex), V the tangential wind speed, and R the radius of curvature. In a saturated environment, as almost fulfilled in the current case, changes in buoyancy due to latent heat release are taken into account by replacing N with its expression for a saturated environment N_m , as defined in Durran and Klemp (1982). Since λ_R depends inversely on f , the time the atmosphere requires to balance the introduced disturbance is longer in the tropics than in midlatitudes for a given basic state. Using an approximate depth of the vortex (i.e., 700 hPa or $H = 3 \text{ km}$), an estimated curvature radius of 200 km (cf. Fig. 10) and box-averaged values for ζ , f , and V , Eq. (4) yield values for λ_R as indicated in Figs. 11e–h. Throughout the MCS passage and the development of the vortex, λ_R is drastically reduced by a few hundreds of kilometers down to 200 km at 0600 UTC 12 June. The implication of the

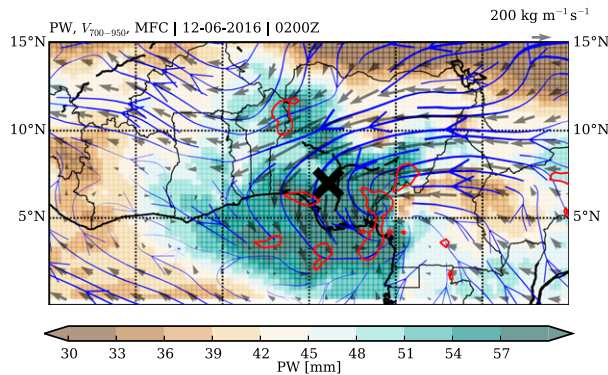


FIG. 10. Precipitable water (PW, color shaded), moisture flux (vectors), 700–950-hPa mass-weighted flow ($V_{700-950}$, blue streamlines), and moisture flux convergence (MFC, red contours) are shown for 0200 UTC 12 Jun. The contours for MFC outline areas with values $>100 \text{ mm day}^{-1}$. The black \times mark denotes the MCS's position.

lowered λ_R is that the required horizontal length scale of the MCS to develop a quasi-balanced flow (i.e., the vortex) is decreased as well. Thus, judging from the size of the MCS, it has become “dynamically large” (e.g., Ooyama 1982; Cotton et al. 1989). In the present case, the lowering of λ_R is realized by virtue of decreasing the moist static stability (i.e., lower N_m , not shown) and gradually increasing the background relative vorticity through MCS dynamics and the synoptic-scale wave over the depth of the (closed) vortex (Figs. 11a–d). The subsequent MCS–vortex interaction becomes a distinct feature of the coastal phase as well.

6. The coastal phase (CP)

Figure 12 shows a Hovmöller diagram during the westward translation along the Guinea Coast from 1200 UTC 11 June and 1000 UTC 4 June 2016, regarding the 3° – 7°N averaged and 600–950-hPa mass-weighted meridional wind (colored), the positive zonal wind (green contours), and the positive relative vorticity (black contours) to highlight the vortex center. The formation of the vortex over the Abakaliki region (around 7° – 9°E) is evident from the pronounced dipole in meridional wind as well as the strong signal in positive relative vorticity after 0000 UTC 12 June. The MCS at snapshot 5 (indicated with “5” in Fig. 12) is located in the periphery of the vortex to its west within northerly and westerly flow. The latter likely results in the distinct curvature of the MCS with a trailing southern flank (Fig. 2b). However, it becomes apparent that the MCS is accompanied by a secondary vortex toward snapshot 6, which separates from the western flank of the main vortex (not shown) and

eventually attains a zonal translation speed similar to the MCS of around -11.4 m s^{-1} . The MCS remains ahead (i.e., west of both vortex centers) at all times. Interestingly, the main vortex moves westward at a substantially slower zonal speed of around -5.5 m s^{-1} . It remains strong throughout 12 June and then dissipates in the early morning of 13 June.

The possible cause behind the formation of the secondary vortex and its link to the MCS is discussed in Fig. 13, which shows vertical cross sections of potential vorticity (PV), vertical velocity and MFC along the latitude of the genesis region (6°N) at 1800 UTC 12 June 2016. The PV profile clearly features a midlevel anomaly couplet of deep vertical extent at 2°E , which is maximized in the midlevels (Fig. 13a). Rather than stability effects, this couplet is primarily generated by anomalies in relative vorticity (see white contours). The PV couplet is further associated with a distinct updraft (Fig. 13b) related to the MCS in ERA5. Therefore, the latter slightly lags behind the MCS seen in observations at this time step. This is consistent with the findings of Elless and Torn (2018), who show that composited ECMWF model rainfall lags observed rainfall from TRMM. A PV couplet of this kind is a typical sign for enhanced tilting (Montgomery et al. 2006). In fact, applying the VTE in the genesis region reveals a strong positive contribution of TILT with a maximum at around 700 hPa (not shown). Additionally, pronounced MFC prevails below the height of the strongest updraft (Fig. 13c). Thus, part of the positive PV anomaly is likely produced by latent heating as well as vortex stretching. As the PV couplet migrates westward at subsequent time steps (not shown), the proposed processes are a strong indication for the MCS–vortex interaction and resemble mechanisms described in Tomassini et al. (2017) and Tomassini (2018).

Similar to Fig. 5, the environmental conditions along the MCS track during the CP are illustrated in Fig. 14, again timed 2 h prior to the MCSs' arrival. Following the discussion about vortex tilting, a prerequisite for high values of TILT is strong LLWS. Here, LLWS ahead of the vortex is distinctively higher than the long-term mean in the region and also clearly exceeds the propagation speed of the MCS along the Guinea Coast (see Fig. 2a). Thus, unlike during the squall line stage, we suggest that the role of LLWS during CP is mainly the production of horizontal vorticity for tilting. The location at MCS snapshot 5 roughly marks the transition from land to ocean and is characterized by a distinct decrease of CAPE by over 1000 J kg^{-1} . It is caused by anomalously dry low levels, which becomes evident through a similar decrease in equivalent potential temperature (θ_e) averaged over the lowest 100 hPa. Simultaneously, a marked drop in 650-hPa-based DCAPE

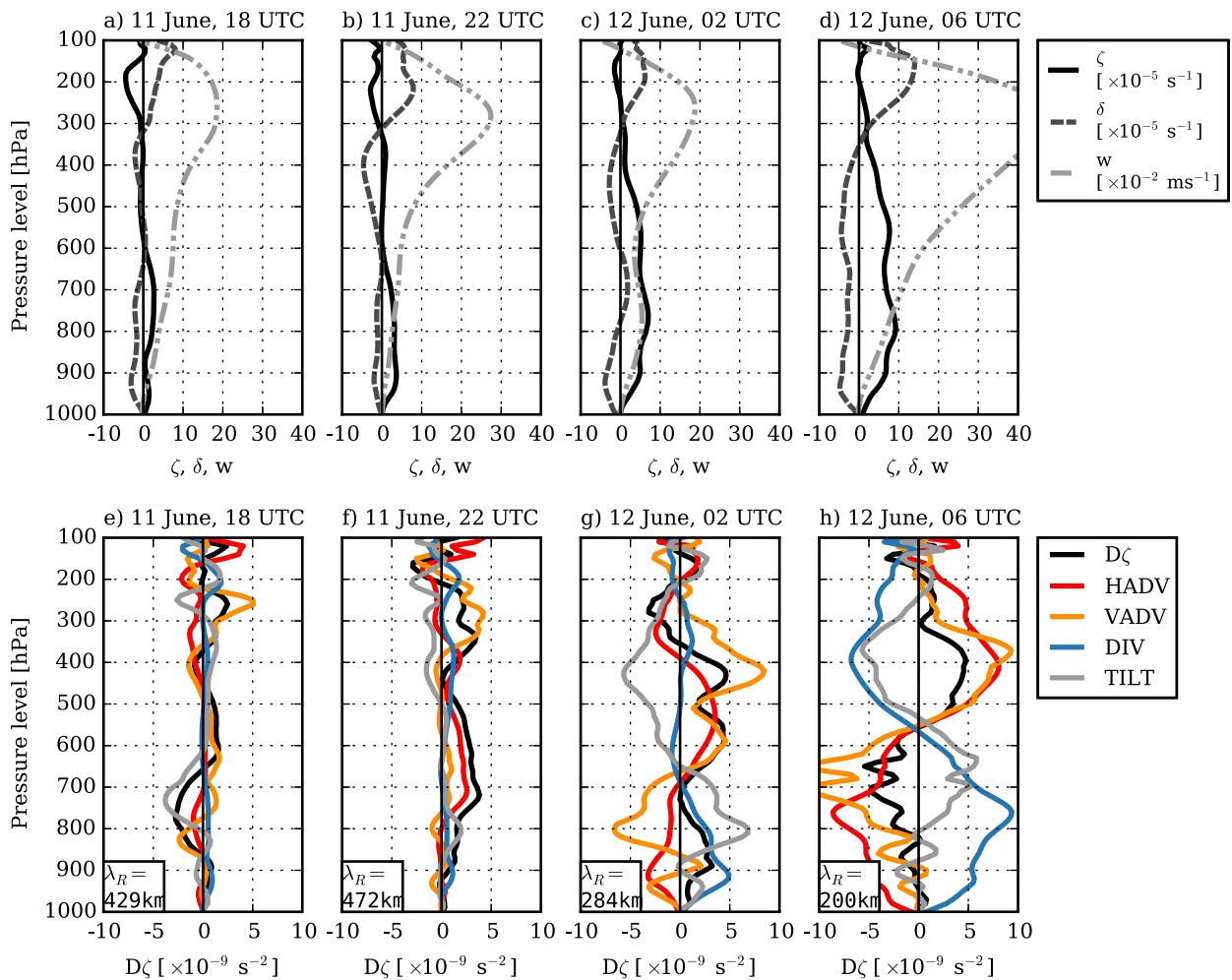


FIG. 11. (a)–(d) Vertical profiles of relative vorticity ζ , divergence δ , and vertical velocity w averaged over the Abakaliki box (see Fig. 1) for four time steps during the MCS passage (1800 UTC 11 Jun–0600 UTC 12 Jun). (e)–(h) Hourly contribution of VTE components to the change in relative vorticity ($D\zeta$, black line) at the same time steps as in (a). The values in the lower left corner indicate the Rossby radius of deformation.

indicates a potentially weaker convective outflow compared to SP due to a moistening of the lower midlevels. Thus, PW remains fairly constant and extreme along the MCS track with values around its 99th percentile. These conditions suggest that MCS maintenance in the coastal region is supported by lifting the moist layer, which is likely realized by constant MFC in around the vortex in a generally low-CIN environment throughout CP (Fig. 14).

7. Summary and conclusions

The present paper investigated (thermo-)dynamic controls of an extreme rainfall event along the Guinea Coast during the DACCIWA field campaign [feature B in Knippertz et al. (2017)], which caused one of the highest ever recorded daily rainfall accumulations at

near-coastal stations in the Guinea Coast region with 223.5 mm at the southern Nigerian station Abakaliki on 12 June 2016. It was caused by an intense, long-lived MCS. Three stages in its life cycle were analyzed using a combination of DACCIWA measurements, satellite observations, and ERA5 reanalysis data. The salient developments and dynamic features, which are summarized in Fig. 15, are:

- The Savannah phase (SP, 1300 UTC 10 June–1200 UTC 11 June) was characterized by the development of a classical West African squall line. After being initiated over the Darfur Mountains due to diurnal heating, the MCS quickly moved southwestward toward Nigeria in a region of midlevel northeasterlies within a broad synoptic-scale trough. The upscale growth into a squall line coincided with pronounced

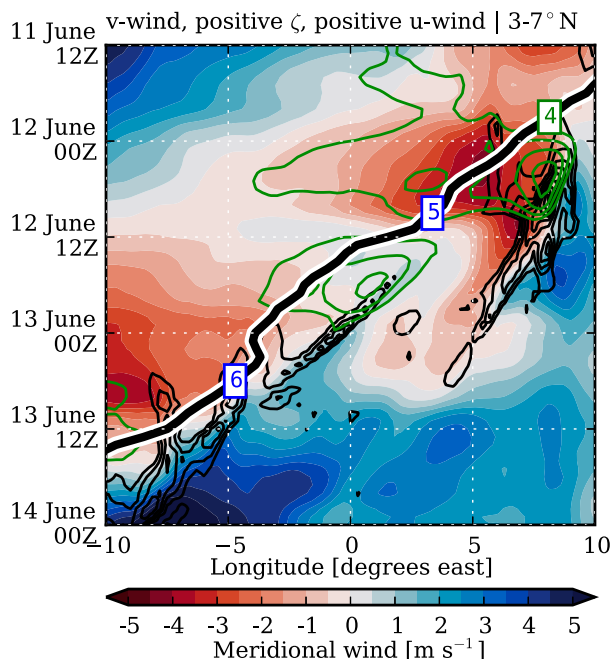


FIG. 12. Hovmöller diagram of meridional wind (color shaded), positive relative vorticity (black contours), and positive zonal wind (green contours) from 1200 UTC 11 Jun to 0000 UTC 14 Jun averaged in the 3°–7°N band and over the 600–950-hPa layer. The black contours start at $2 \times 10^{-5} \text{ s}^{-1}$ incremented by 10^{-5} s^{-1} , the green contours at 1 m s^{-1} incremented by 1 m s^{-1} . The numbers on the MCS track correspond to the MCS snapshots shown in Fig. 2.

LLWS between the northeasterlies and the undercutting westerly NLLJ as well as dry midlevels. The latter usually favors a strong convective downdraft and surface outflow, and might have supported convective organization. (Fig. 15f, left). Furthermore, increasing CAPE and PW values were detected along the southwestward MCS track.

- The Nigerian phase (NP, 1200 UTC 11 June –0600 UTC 12 June) culminated in a strong intensification of the squall line and the associated formation of a moist vortex over the Abakaliki region. The intensification was promoted by an extremely moist lower troposphere (total PW > 99th percentile), which was established by strong MFC (peak at 140 mm day^{-1}) prior to the arrival of the squall line. A short-lived local heat low, causing the high MFC, formed mainly as a consequence of MCS-forced subsidence and further column warming due to insolation according to the PTE (see also Fig. 15f, middle). As indicated by the VTE, the intensification of the MCS in this moist environment led to a substantial production of cyclonic vorticity in the column above the heat low due to vortex stretching and vertical vorticity advection. The passage of the midlevel trough further deepened the layer of cyclonic vorticity. The gradual decrease of the Rossby radius of deformation suggests that the spatial extent of the MCS became large enough to enable the formation of a lower-tropospheric vortex, which in turn was capable of both trapping moisture and slowing down the propagation of the MCS. The latter supported the extreme rainfall accumulation over Abakaliki.
- During the coastal phase (CP, 0600 UTC 12 June –1800 UTC 13 June), a secondary vortex separated from the western flank of the main vortex likely due to vortex tilting and stretching associated with the MCS. Subsequent convective activity was closely linked to this secondary vortex traveling along the Guinea Coast. Lower DCAPE values during CP compared to SP due to moist midlevels indicate potentially weaker cold pools. Thus, MCS maintenance is suggested to be particularly realized through constant MFC and lifting

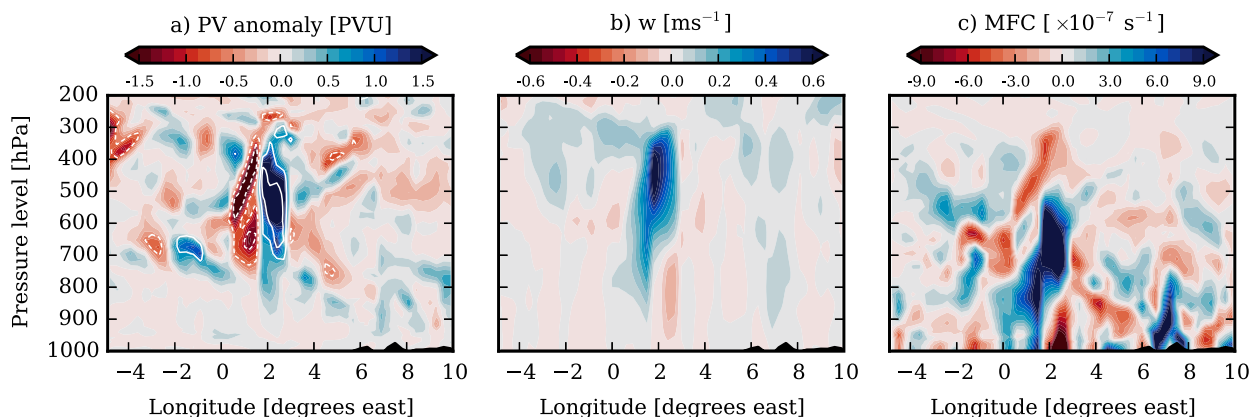


FIG. 13. Zonally oriented vertical cross sections of (a) potential vorticity, (b) vertical velocity, and (c) MFC along 6°N at 1800 UTC 12 Jun. Orographic features are shaded in black. The white solid (dashed) contours in (a) denote anomalies in positive (negative) relative vorticity, starting at $\pm 1 \times 10^{-4} \text{ s}^{-1}$ and incremented by $\pm 1 \times 10^{-4} \text{ s}^{-1}$.

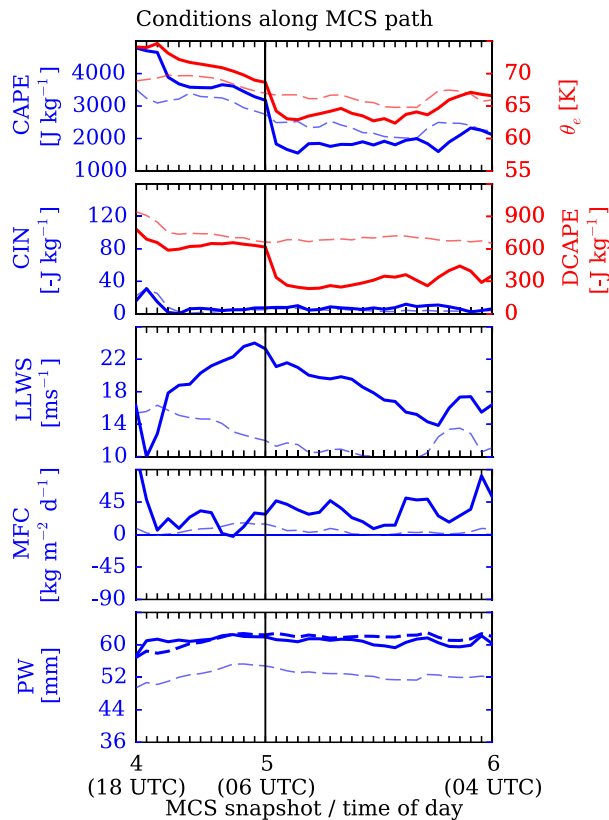


FIG. 14. As in Fig. 5, but between MCS snapshot locations 4 and 6 (see Fig. 2). The equivalent potential temperature (θ_e), averaged over the lowest 100 hPa, was added to the panel of CAPE.

associated with the secondary vortex, which itself is maintained through vorticity generation by the MCS.

A vortex formation due to an MCS passage and the subsequent coupling between vortex and MCS has rarely been documented in detail for the Guinea Coast region. Substantial work on this topic has been dedicated to the midlatitudes (e.g., Cotton et al. 1989; Knievel and Johnson 2003; Galarneau et al. 2009), where more conducive conditions for the developments of mesoscale convective vortices prevail than in the tropics due to the higher background planetary vorticity. This is a major element of the concept of λ_R , which was significantly lowered during the MCS passage. Thus, we propose that the MCS became “dynamically large” at some point (i.e., larger than λ_R , which facilitated the vortex formation by the MCS). In principle, Cotton et al. (1989) already pointed out that larger modifications to the inertial stability around MCSs in tropical regions is primarily subject to the areal extent of an MCS and/or the presence of substantial rotation within it. The present case outlined the dimensions under which a quasi-balanced vortex is able to form in a low-latitude region such as the humid Guinea Coast.

Although not directly located in the moist Guinea Coast region, at least two cases of vortex generations are documented for the Sahelian and Soudanian bands farther north, showing some parallels to the dynamical characteristics over the Abakaliki region. First, the high-impact rainfall event around Ouagadougou 2009 in the Sudanian zone was caused by the passage of two successive convective cells within a moist vortex, the latter of which developed from a “breaking” AEW (Galvin 2010; Lafore et al. 2017; Engel et al. 2017). Together with their slow-moving behavior, the (thermo-) dynamical implications associated with these vortices, such as trapped moisture and high MFC, appear to be favorable ingredients for local rainfall amounts beyond 200 mm, irrespective of the climatic zone within West Africa. However, judging by the high moisture availability, such extreme rainfall events in the Guinea Coast region may generally not require the high intensity of the vortex in the Ouagadougou case. In the second case, Schwendike and Jones (2010) investigated the dynamic controls leading to the precursor of Hurricane Helene in 2006, which was influenced by strong vortex stretching due to the superposition of a low-level cyclonic circulation and a midlevel AEW anomaly. Although mostly driven by the MCS in the present case, vortex stretching also occurred with a preexisting low-level depression (Fig. 15f, middle) and was further supported by the passage of the mid- to low-level trough. The similarities in the succession of these dynamic characteristics for vortex development are quite intriguing and require more in-depth studies in the future, especially with respect to their roles for extreme rainfall.

For the subsequent MCS maintenance in the moist Guinea Coast region, the (secondary) vortex is suggested to play a major role. Although such midlevel vortices have been linked to prolonged rainfall (Acheampong 1982; Buckle 1996; Fink et al. 2006), cases of mesoscale vortices coupling with MCSs at the Guinea Coast have rarely been reported, if at all. Thus, there is no established theory for MCS maintenance in this region. However, some of our findings bear resemblance to mechanisms in studies, which dealt with the maintenance of MCSs. In their theory about long-lived MCSs, Raymond and Jiang (1990) postulated a mechanism of forced ascent involving a positive low- to midlevel PV anomaly and ambient wind shear, where lifting is promoted both underneath and on the downshear side of the PV anomaly. Assuming easterly shear like in the present case, strongest lifting therefore occurs effectively to the west of the PV anomaly (Fig. 15f, right), which would fit the observation (Fig. 12). The MCS can be maintained as long as high moisture content

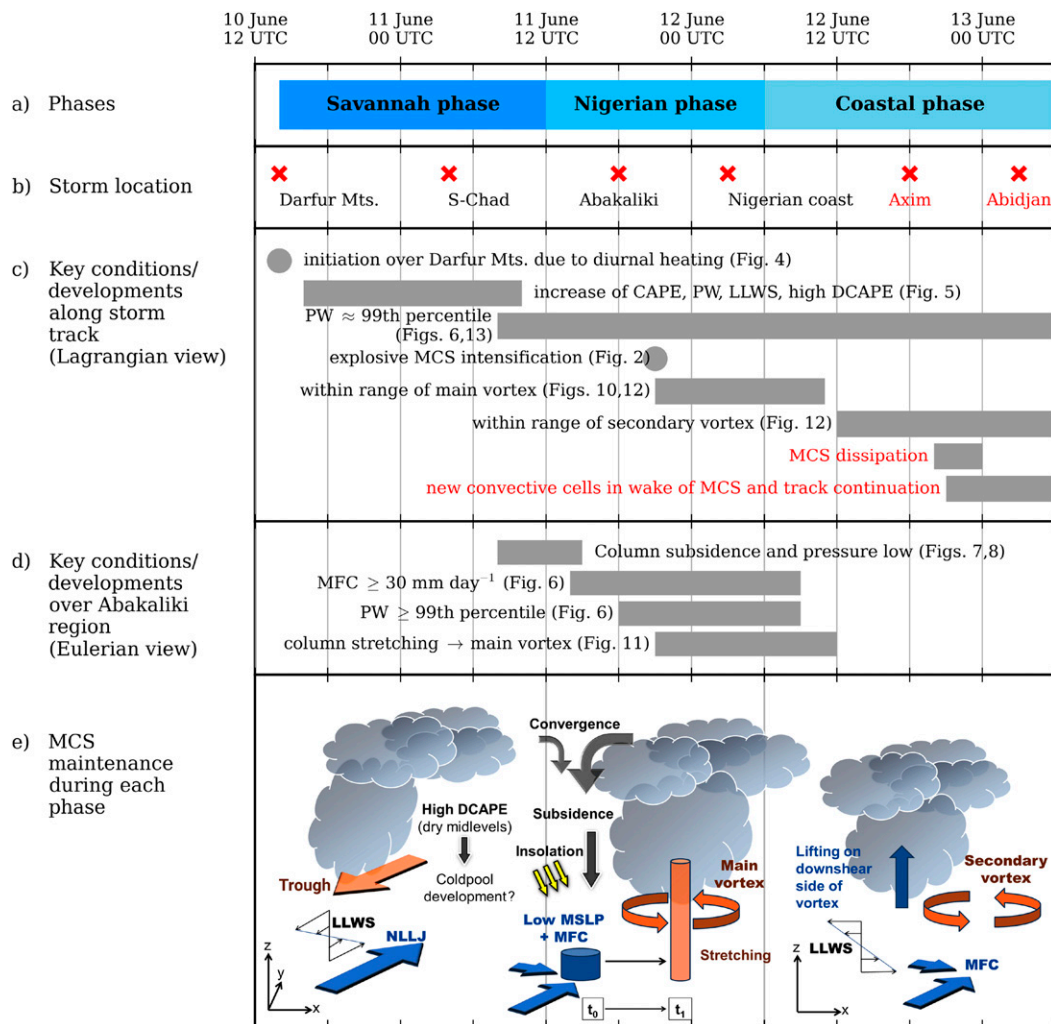


FIG. 15. Schematic summary of the evolution of the extreme rainfall event in a timeline encompassing 1200 UTC 10 Jun 2016 and 0600 UTC 13 Jun 2016 and containing (a) the three phases of MCS development discussed in this paper, (b) the location of the storm, (c),(d) key conditions and developments along the storm track and over the Abakaliki region, respectively, and (e) proposed mechanisms for MCS maintenance during the different phases with more details in section 7. In (c) and (d), the gray bars denote the length of the periods. Furthermore, references to figures are given. The red-colored text indicates events mentioned in the text, but not explicitly analyzed.

and unstable air masses are reestablished and lifted (Markowski and Richardson 2011), which may explain why the MCS was tied so closely to the vortex. Conversely, the long lifetime of the vortex is likely related to the MCS to some extent. Such a two-way interaction is described in a similar fashion in Tomassini et al. (2017), who investigated mechanisms on the maintenance of both MCS and AEW. In essence, while the AEW promotes moisture convergence ahead of the trough axis in the region of the MCS, diabatic heating and subsequent vortex stretching within the MCS leads to the production of cyclonic vorticity. This, in turn, facilitates the propagation of both MCS and AEW, which was further analyzed in a follow-up modeling study by Tomassini

(2018). Clearly, similar modeling work may provide more insight into the MCS–vortex interaction for this case study, too.

Finally, this case study visualized the susceptibility to extreme rainfall events over the Guinea Coast region under extraordinary humid conditions. Since changes in extreme rainfall amounts associated with climate change have been proposed to scale with the moisture content according to the Clausius–Clapeyron equation (Westra et al. 2013; Lehmann et al. 2015), particularly in the large convergence zones in the tropics (Trenberth et al. 2003; Trenberth 2011), it remains to be answered whether such phenomena will become more frequent in the future. The implications of changes in the (thermo-)dynamical fields,

such as a potential gradual reduction of λ_R , warrant further studies, not least since southern West Africa is currently experiencing rapid demographic changes.

Acknowledgments. The DACCIWA project has received funding from the European Union Seventh Framework Programme (FP7/2007-2013) under grant agreement no. 603502 (EU project DACCIWA: Dynamics-aerosol-chemistry-cloud interactions in West Africa). Rainfall time series from various West African stations used in this manuscript were obtained from the Karlsruhe African Surface Station-Database (KASS-D) from the Institute of Meteorology and Climate Research of the Karlsruhe Institute of Technology, Germany. The AMMA-CATCH regional observing system (<http://www.amma-catch.org>) was set up thanks to an incentive funding of the French Ministry of Research that allowed pooling together various preexisting small scale observing setups. The continuity and long-term perenity of the measurements are made possible by an undisrupted IRD funding since 1990 and by a continuous CNRS-INSU funding since 2005. Finally, we want to acknowledge Dr. Matthew A. Janiga and the two anonymous reviewers for their constructive comments that helped to improve this manuscript.

REFERENCES

- Acheampong, P. K., 1982: Rainfall anomaly along the coast of Ghana. Its nature and causes. *Geogr. Ann.*, **64A**, 199–211, <https://doi.org/10.2307/520646>.
- Alexander, L., and Coauthors, 2006: Global observed changes in daily climate extremes of temperature and precipitation. *J. Geophys. Res.*, **111**, D05109, <https://doi.org/10.1029/2005JD006290>.
- Barnes, G., and K. Sieckman, 1984: The environment of fast-and slow-moving tropical mesoscale convective cloud lines. *Mon. Wea. Rev.*, **112**, 1782–1794, [https://doi.org/10.1175/1520-0493\(1984\)112<1782:TEOFAS>2.0.CO;2](https://doi.org/10.1175/1520-0493(1984)112<1782:TEOFAS>2.0.CO;2).
- Berry, G. J., and C. Thorncroft, 2005: Case study of an intense African easterly wave. *Mon. Wea. Rev.*, **133**, 752–766, <https://doi.org/10.1175/MWR2884.1>.
- Buckle, C., 1996: *Weather and Climate in Africa*. Longman, 312 pp.
- Cotton, W. R., M.-S. Lin, R. L. McAnelly, and C. J. Tremback, 1989: A composite model of mesoscale convective complexes. *Mon. Wea. Rev.*, **117**, 765–783, [https://doi.org/10.1175/1520-0493\(1989\)117<0765:ACMOMC>2.0.CO;2](https://doi.org/10.1175/1520-0493(1989)117<0765:ACMOMC>2.0.CO;2).
- D'Amato, N., and T. Lebel, 1998: On the characteristics of the rainfall events in the Sahel with a view to the analysis of climatic variability. *Int. J. Climatol.*, **18**, 955–974, [https://doi.org/10.1002/\(SICI\)1097-0088\(199807\)18:9<955::AID-JOC236>3.0.CO;2-6](https://doi.org/10.1002/(SICI)1097-0088(199807)18:9<955::AID-JOC236>3.0.CO;2-6).
- Davis, C. A., and T. J. Galarneau Jr., 2009: The vertical structure of mesoscale convective vortices. *J. Atmos. Sci.*, **66**, 686–704, <https://doi.org/10.1175/2008JAS2819.1>.
- Dee, D. P., and Coauthors, 2011: The ERA-Interim reanalysis: Configuration and performance of the data assimilation system. *Quart. J. Roy. Meteor. Soc.*, **137**, 553–597, <https://doi.org/10.1002/qj.828>.
- Di Baldassarre, G., A. Montanari, H. Lins, D. Koutsoyiannis, L. Brandimarte, and G. Blöschl, 2010: Flood fatalities in Africa: From diagnosis to mitigation. *Geophys. Res. Lett.*, **37**, L22402, <https://doi.org/10.1029/2010GL045467>.
- Donat, M., and Coauthors, 2013: Updated analyses of temperature and precipitation extreme indices since the beginning of the twentieth century: The HadEX2 dataset. *J. Geophys. Res. Atmos.*, **118**, 2098–2118, <https://doi.org/10.1002/jgrd.50150>.
- Durran, D. R., and J. B. Klemp, 1982: On the effects of moisture on the Brunt–Väisälä frequency. *J. Atmos. Sci.*, **39**, 2152–2158, [https://doi.org/10.1175/1520-0469\(1982\)039<2152:OTEOMO>2.0.CO;2](https://doi.org/10.1175/1520-0469(1982)039<2152:OTEOMO>2.0.CO;2).
- Easterling, D. R., J. Evans, P. Ya. Groisman, T. R. Karl, K. E. Kunkel, and P. Ambenje, 2000: Observed variability and trends in extreme climate events: A brief review. *Bull. Amer. Meteor. Soc.*, **81**, 417–426, [https://doi.org/10.1175/1520-0477\(2000\)081<0417:OVATIE>2.3.CO;2](https://doi.org/10.1175/1520-0477(2000)081<0417:OVATIE>2.3.CO;2).
- Elless, T. J., and R. D. Torn, 2018: African easterly wave forecast verification and its relation to convective errors within the ECMWF ensemble prediction system. *Wea. Forecasting*, **33**, 461–477, <https://doi.org/10.1175/WAF-D-17-0130.1>.
- Emanuel, K. A., 1994: *Atmospheric Convection*. Oxford University Press, 580 pp.
- Engel, T., A. Fink, and P. Knippertz, 2017: Extreme flooding in the West African cities of Dakar and Ouagadougou—Atmospheric dynamics and implications for flood risk assessments. *Geophysical Research Abstracts*, Vol. 19, Abstract 11983, <https://meetingorganizer.copernicus.org/EGU2017/EGU2017-11983.pdf>.
- EUMETSAT, 2015: Divergence product: Product guide. Tech. Rep. EUM/TSS/MAN/15/795706 v1C, 10 pp.
- Fink, A. H., D. Vincent, and V. Ermert, 2006: Rainfall types in the West African Sudanian zone during the summer monsoon 2002. *Mon. Wea. Rev.*, **134**, 2143–2164, <https://doi.org/10.1175/MWR3182.1>.
- , S. Pohle, J. G. Pinto, and P. Knippertz, 2012: Diagnosing the influence of diabatic processes on the explosive deepening of extratropical cyclones. *Geophys. Res. Lett.*, **39**, L07803, <https://doi.org/10.1029/2012GL051025>.
- Fortune, M., 1980: Properties of African squall lines inferred from time-lapse satellite imagery. *Mon. Wea. Rev.*, **108**, 153–168, [https://doi.org/10.1175/1520-0493\(1980\)108<0153:POASLI>2.0.CO;2](https://doi.org/10.1175/1520-0493(1980)108<0153:POASLI>2.0.CO;2).
- Galarneau, T. J., Jr., L. F. Bosart, C. A. Davis, and R. McTaggart-Cowan, 2009: Baroclinic transition of a long-lived mesoscale convective vortex. *Mon. Wea. Rev.*, **137**, 562–584, <https://doi.org/10.1175/2008MWR2651.1>.
- Galvin, J., 2010: Two easterly waves in West Africa in summer 2009. *Weather*, **65**, 219–227, <https://doi.org/10.1002/wea.605>.
- Hastings, D. A., and Coauthors, 1999: The Global Land One-Kilometer Base Elevation (GLOBE) digital elevation model, version 1.0. National Oceanic and Atmospheric Administration, National Geophysical Data Center, accessed 15 September 2018, <http://www.ngdc.noaa.gov/mgg/topo/globe.html>.
- Hersbach, H., and D. Dee, 2016: ERA5 reanalysis is in production. *ECMWF Newsletter*, Vol. 147, ECMWF, Reading, United Kingdom, 7, <http://www.ecmwf.int/sites/default/files/elibrary/2016/16299-newsletter-no147-spring-2016.pdf>.
- Holton, J. R., and G. J. Hakim, 2012: *An Introduction to Dynamic Meteorology*. Academic Press, 552 pp.
- Hou, A. Y., and Coauthors, 2014: The global precipitation measurement mission. *Bull. Amer. Meteor. Soc.*, **95**, 701–722, <https://doi.org/10.1175/BAMS-D-13-00164.1>.
- Huffman, G. J., D. T. Bolvin, D. Braithwaite, K. Hsu, R. Joyce, P. Xie, and S.-H. Yoo, 2015: NASA global precipitation measurement (GPM) integrated multi-satellite retrievals for

- GPM (IMERG). Algorithm Theoretical Basis Document, version 4, 30 pp.
- Janiga, M. A., and C. D. Thorncroft, 2014: Convection over tropical Africa and the east Atlantic during the West African monsoon: Regional and diurnal variability. *J. Climate*, **27**, 4159–4188, <https://doi.org/10.1175/JCLI-D-13-00449.1>.
- Kamara, S. I., 1986: The origins and types of rainfall in West Africa. *Weather*, **41**, 48–56, <https://doi.org/10.1002/j.1477-8696.1986.tb03787.x>.
- Kniviel, J. C., and R. H. Johnson, 2003: A scale-discriminating vorticity budget for a mesoscale vortex in a midlatitude, continental mesoscale convective system. *J. Atmos. Sci.*, **60**, 781–794, [https://doi.org/10.1175/1520-0469\(2003\)060<0781:ASDVBF>2.0.CO;2](https://doi.org/10.1175/1520-0469(2003)060<0781:ASDVBF>2.0.CO;2).
- Knippertz, P., and A. H. Fink, 2008: Dry-season precipitation in tropical West Africa and its relation to forcing from the extratropics. *Mon. Wea. Rev.*, **136**, 3579–3596, <https://doi.org/10.1175/2008MWR2295.1>.
- , —, R. Schuster, J. Trentmann, J. M. Schrage, and C. Yorke, 2011: Ultra-low clouds over the southern West African monsoon region. *Geophys. Res. Lett.*, **38**, L21808, <https://doi.org/10.1029/2011GL049278>.
- , and Coauthors, 2015: The DACCIWA project: Dynamics–aerosol–chemistry–cloud interactions in West Africa. *Bull. Amer. Meteor. Soc.*, **96**, 1451–1460, <https://doi.org/10.1175/BAMS-D-14-00108.1>.
- , and Coauthors, 2017: A meteorological and chemical overview of the DACCIWA field campaign in West Africa in June–July 2016. *Atmos. Chem. Phys.*, **17**, 10 893–10 918, <https://doi.org/10.5194/acp-17-10893-2017>.
- Lafore, J.-P., and Coauthors, 2017: A multi-scale analysis of the extreme rain event of Ouagadougou in 2009. *Quart. J. Roy. Meteor. Soc.*, **143**, 3094–3109, <https://doi.org/10.1002/qj.3165>.
- Laing, A. G., R. Carbone, V. Levizzani, and J. Tuttle, 2008: The propagation and diurnal cycles of deep convection in northern tropical Africa. *Quart. J. Roy. Meteor. Soc.*, **134**, 93–109, <https://doi.org/10.1002/qj.194>.
- Lebel, T., and A. Ali, 2009: Recent trends in the central and western Sahel rainfall regime (1990–2007). *J. Hydrol.*, **375**, 52–64, <https://doi.org/10.1016/j.jhydrol.2008.11.030>.
- Lehmann, J., D. Coumou, and K. Frieler, 2015: Increased record-breaking precipitation events under global warming. *Climatic Change*, **132**, 501–515, <https://doi.org/10.1007/s10584-015-1434-y>.
- LeMone, M. A., E. J. Zipser, and S. B. Trier, 1998: The role of environmental shear and thermodynamic conditions in determining the structure and evolution of mesoscale convective systems during TOGA COARE. *J. Atmos. Sci.*, **55**, 3493–3518, [https://doi.org/10.1175/1520-0469\(1998\)055<3493:TROESA>2.0.CO;2](https://doi.org/10.1175/1520-0469(1998)055<3493:TROESA>2.0.CO;2).
- Lothon, M., F. Saïd, F. Lohou, and B. Campistron, 2008: Observation of the diurnal cycle in the low troposphere of West Africa. *Mon. Wea. Rev.*, **136**, 3477–3500, <https://doi.org/10.1175/2008MWR2427.1>.
- Maranan, M., and A. H. Fink, 2016: Radiosonde—All sites. Sedoo/Baobab database, accessed 30 March 2017, <https://doi.org/10.6096/BAOBAB-DACCIWA.1656>.
- , —, and P. Knippertz, 2018: Rainfall types over southern West Africa: Objective identification, climatology and synoptic environment. *Quart. J. Roy. Meteor. Soc.*, **144**, 1628–1648, <https://doi.org/10.1002/qj.3345>.
- Markowski, P., and Y. Richardson, 2011: *Mesoscale Meteorology in Midlatitudes*. John Wiley & Sons, 430 pp.
- Mathon, V., and H. Laurent, 2001: Life cycle of Sahelian mesoscale convective cloud systems. *Quart. J. Roy. Meteor. Soc.*, **127**, 377–406, <https://doi.org/10.1002/qj.49712757208>.
- , —, and T. Lebel, 2002: Mesoscale convective system rainfall in the Sahel. *J. Appl. Meteor.*, **41**, 1081–1092, [https://doi.org/10.1175/1520-0450\(2002\)041<1081:MCSRIT>2.0.CO;2](https://doi.org/10.1175/1520-0450(2002)041<1081:MCSRIT>2.0.CO;2).
- Mekonnen, A., C. D. Thorncroft, and A. R. Aiyyer, 2006: Analysis of convection and its association with African easterly waves. *J. Climate*, **19**, 5405–5421, <https://doi.org/10.1175/JCLI3920.1>.
- Montgomery, M., M. Nicholls, T. Cram, and A. Saunders, 2006: A vortical hot tower route to tropical cyclogenesis. *J. Atmos. Sci.*, **63**, 355–386, <https://doi.org/10.1175/JAS3604.1>.
- Nesbitt, S. W., R. Cifelli, and S. A. Rutledge, 2006: Storm morphology and rainfall characteristics of TRMM precipitation features. *Mon. Wea. Rev.*, **134**, 2702–2721, <https://doi.org/10.1175/MWR3200.1>.
- Nicholson, S., 2005: On the question of the “recovery” of the rains in the West African Sahel. *J. Arid Environ.*, **63**, 615–641, <https://doi.org/10.1016/j.jaridenv.2005.03.004>.
- , 2009: On the factors modulating the intensity of the tropical rainbelt over West Africa. *Int. J. Climatol.*, **29**, 673–689, <https://doi.org/10.1002/joc.1702>.
- Nka, B., L. Oudin, H. Karambiri, J.-E. Paturel, and P. Ribstein, 2015: Trends in floods in West Africa: Analysis based on 11 catchments in the region. *Hydrol. Earth Syst. Sci.*, **19**, 4707–4719, <https://doi.org/10.5194/hess-19-4707-2015>.
- Omotosho, J. B., 1984: Spatial and seasonal variation of line squalls over West Africa. *Arch. Meteor. Geophys. Bioclimatol.*, **33A**, 143–150, <https://doi.org/10.1007/bf02257721>.
- , 1985: The separate contributions of line squalls, thunderstorms and the monsoon to the total rainfall in Nigeria. *Int. J. Climatol.*, **5**, 543–552, <https://doi.org/10.1002/joc.3370050507>.
- Ooyama, K. V., 1982: Conceptual evolution of the theory and modeling of the tropical cyclone. *J. Meteor. Soc. Japan*, **60**, 369–380, https://doi.org/10.2151/jmsj1965.60.1_369.
- Paeth, H., A. H. Fink, S. Pohle, F. Keis, H. Mächel, and C. Samimi, 2011: Meteorological characteristics and potential causes of the 2007 flood in sub-Saharan Africa. *Int. J. Climatol.*, **31**, 1908–1926, <https://doi.org/10.1002/joc.2199>.
- Panthou, G., T. Vischel, and T. Lebel, 2014: Recent trends in the regime of extreme rainfall in the central Sahel. *Int. J. Climatol.*, **34**, 3998–4006, <https://doi.org/10.1002/joc.3984>.
- Parker, D. J., C. D. Thorncroft, R. R. Burton, and A. Diongue-Niang, 2005: Analysis of the African easterly jet, using aircraft observations from the JET2000 experiment. *Quart. J. Roy. Meteor. Soc.*, **131**, 1461–1482, <https://doi.org/10.1256/qj.03.189>.
- Raymond, D., and H. Jiang, 1990: A theory for long-lived mesoscale convective systems. *J. Atmos. Sci.*, **47**, 3067–3077, [https://doi.org/10.1175/1520-0469\(1990\)047<3067:ATFLLM>2.0.CO;2](https://doi.org/10.1175/1520-0469(1990)047<3067:ATFLLM>2.0.CO;2).
- Redl, R., A. H. Fink, and P. Knippertz, 2015: An objective detection method for convective cold pool events and its application to northern Africa. *Mon. Wea. Rev.*, **143**, 5055–5072, <https://doi.org/10.1175/MWR-D-15-0223.1>.
- Rotunno, R., J. B. Klemp, and M. L. Weisman, 1988: A theory for strong, long-lived squall lines. *J. Atmos. Sci.*, **45**, 463–485, [https://doi.org/10.1175/1520-0469\(1988\)045<463:ATFSLM>2.0.CO;2](https://doi.org/10.1175/1520-0469(1988)045<463:ATFSLM>2.0.CO;2).
- Sanogo, S., A. H. Fink, J. A. Omotosho, A. Ba, R. Redl, and V. Ermert, 2015: Spatio-temporal characteristics of the recent rainfall recovery in West Africa. *Int. J. Climatol.*, **35**, 4589–4605, <https://doi.org/10.1002/joc.4309>.
- Schrage, J. M., and A. H. Fink, 2012: Nocturnal continental low-level stratus over tropical West Africa: Observations and possible mechanisms controlling its onset. *Mon. Wea. Rev.*, **140**, 1794–1809, <https://doi.org/10.1175/MWR-D-11-00172.1>.

- Schröder, M., M. König, and J. Schmetz, 2009: Deep convection observed by the spinning enhanced visible and infrared imager on board Meteosat 8: Spatial distribution and temporal evolution over Africa in summer and winter 2006. *J. Geophys. Res.*, **114**, D05109, <https://doi.org/10.1029/2008JD010653>.
- Schwendike, J., and S. C. Jones, 2010: Convection in an African easterly wave over West Africa and the eastern Atlantic: A model case study of Helene (2006). *Quart. J. Roy. Meteor. Soc.*, **136**, 364–396, <https://doi.org/10.1002/qj.566>.
- Subrahmanyam, K., and K. Kumar, 2013: Megha-Tropiques/SAPHIR measurements of humidity profiles: Validation with AIRS and global radiosonde network. *Atmos. Meas. Tech. Discuss.*, **6**, 11 405–11 437, <https://doi.org/10.5194/amtd-6-11405-2013>.
- Sui, C.-H., and M. Yanai, 1986: Cumulus ensemble effects on the large-scale vorticity and momentum fields of GATE. Part I: Observational evidence. *J. Atmos. Sci.*, **43**, 1618–1642, [https://doi.org/10.1175/1520-0469\(1986\)043<1618:CEEOTL>2.0.CO;2](https://doi.org/10.1175/1520-0469(1986)043<1618:CEEOTL>2.0.CO;2).
- Tomassini, L., 2018: Mesoscale circulations and organized convection in African easterly waves. *J. Atmos. Sci.*, **75**, 4357–4381, <https://doi.org/10.1175/JAS-D-18-0183.1>.
- , D. J. Parker, A. Stirling, C. Bain, C. Senior, and S. Milton, 2017: The interaction between moist diabatic processes and the atmospheric circulation in African easterly wave propagation. *Quart. J. Roy. Meteor. Soc.*, **143**, 3207–3227, <https://doi.org/10.1002/qj.3173>.
- Trenberth, K. E., 2011: Changes in precipitation with climate change. *Climate Res.*, **47**, 123–138, <https://doi.org/10.3354/cr00953>.
- , A. Dai, R. M. Rasmussen, and D. B. Parsons, 2003: The changing character of precipitation. *Bull. Amer. Meteor. Soc.*, **84**, 1205–1218, <https://doi.org/10.1175/BAMS-84-9-1205>.
- , and Coauthors, 2007: Observations: Surface and atmospheric climate change. *Climate Change 2007: The Physical Science Basis*, S. Solomon et al., Eds., Cambridge University Press, 235–336.
- Weisman, M. L., and J. B. Klemp, 1982: The dependence of numerically simulated convective storms on vertical wind shear and buoyancy. *Mon. Wea. Rev.*, **110**, 504–520, [https://doi.org/10.1175/1520-0493\(1982\)110<0504:TDONSC>2.0.CO;2](https://doi.org/10.1175/1520-0493(1982)110<0504:TDONSC>2.0.CO;2).
- Westra, S., L. V. Alexander, and F. W. Zwiers, 2013: Global increasing trends in annual maximum daily precipitation. *J. Climate*, **26**, 3904–3918, <https://doi.org/10.1175/JCLI-D-12-00502.1>.
- WHO/WFP, 2007: Community-based management of severe acute malnutrition: A Joint Statement by the World Health Organization, the World Food Programme, the United Nations System Standing Committee on Nutrition and the United Nations Children's Fund. WHO/WFP, 7 pp., <https://apps.who.int/iris/handle/10665/44295>.